JCTC Journal of Chemical Theory and Computation

pubs.acs.org/JCTC Review

Ab Initio Predictions of Spin Relaxation, Dephasing, and Diffusion in Solids

Junqing Xu and Yuan Ping*

Cite This: J. Chem. Theory Comput. 2024, 20, 492−512 Read Online

ACCESS | Metrics & More | Article Recommendations

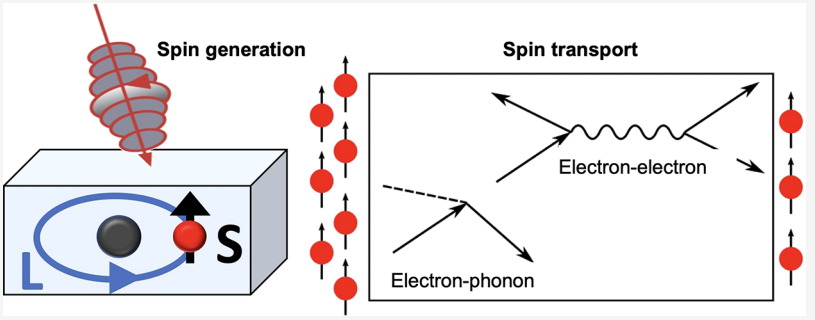

ABSTRACT: Spin relaxation, dephasing, and diffusion are at the heart of spin-based information technology. Accurate theoretical approaches to simulate spin lifetimes (τ_s), determining how fast the spin polarization and phase information will be lost, are important to the understanding of the underlying mechanism of these spin processes, and invaluable in searching for promising candidates of spintronic materials. Recently, we develop a first-principles real-time density-matrix (FPDM) approach to simulate spin dynamics for general solid-state systems. Through the complete first-principles descriptions of light−matter interaction and scattering processes including electron−phonon, electron−impurity, and electron−electron scatterings with self-consistent spin−orbit coupling, as well as ab initio Landé g-factor, our method can predict τ_s at various conditions as a function of carrier density and temperature, under electric and magnetic fields. By employing this method, we successfully reproduce experimental results of disparate materials and identify the key factors affecting spin relaxation, dephasing, and diffusion in different materials. Specifically, we predict that germanene has long τ_s (∼100 ns at 50 K), a giant spin lifetime anisotropy, and spin−valley locking effect under electric fields, making it advantageous for spin−valleytronic applications. Based on our theoretical derivations and ab initio simulations, we propose a new useful electronic quantity, named spin−flip angle $\theta^{\uparrow\downarrow}$, for the understanding of spin relaxation through intervalley spin−flip scattering processes. Our method can be further applied to other emerging materials and extended to simulate exciton spin dynamics and steady-state photocurrents due to photogalvanic effect.

I. INTRODUCTION

In the past two decades, spintronics in unconventional semiconductors and metals, including two-dimensional materials and their heterostructures,[1,2] topological and magnetic materials,[3,4] hybrid perovskites,[5,6] etc., have drawn significant interests owing to its unprecedented potentials in microelectronics and next generation low-power electronics. Spin, as a pure quantum mechanical object, is the fundamental information on carrier instead of charge, with much less energy dissipation. Ideally one wants such information preserved as long as possible for stable manipulation. Therefore, understanding how spins relax and transport is of central importance in spintronics.

Spin is an unconserved quantity in solids due to its coupling with other quantities, such as electron orbital. Therefore, after excess spins being generated, spin can loose its polarization (relaxation) and phase (dephasing) due to coupling with the environment. One critical parameter describing the time scale of such processes is spin lifetime τ_s including T_1 (relaxation) and T_2 (dephasing), which is often required to be sufficiently long for stable detection and manipulation of spin. Accurate and reliable theoretical approaches to simulate τ_s are demanded for the detailed understandings of spin dynamics and transport phenomena, and designing new spintronics materials and devices.

Previously, methods based on model Hamiltonian with empirical parameters[1,7,8] were extensively employed for

Received: June 3, 2023
Revised: December 6, 2023
Accepted: December 6, 2023
Published: December 29, 2023

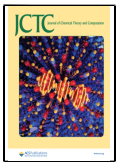

simulation of spin relaxation, dephasing, and diffusion in solids. While these methods provide some mechanistic insight, they do not serve as predictive tools for the design of new materials and may sometimes lead to qualitatively incorrect predictions due to the use of simplified electronic structures and interactions.

To mitigate these issues, several different first-principles approaches were proposed, which often are suitable for particular symmetry or simulation conditions.[9−15] For example, methods considering spin−flip transitions based on Fermi's golden rule (FGR) were implemented to simulate phonon- and impurity-induced spin relaxation,[9,10] which are more proper for Elliot−Yafet mechanism; spin dynamics based on time-dependent density functional theory (TDDFT)[11] was developed for ultrafast demagnetization of magnetic systems, more affordable within a ps process.[12−14] Recently, a method based on spin−spin correlation function was developed to simulate spin−phonon relaxation[15] time, which may be applicable to both Elliot−Yafet and Dyakonov Perel mechanisms, but its generality to various relaxation and dephasing channels as well as their dependence on external conditions remains to be seen.

Recently, we developed a first-principles real-time density-matrix (FPDM) approach[16−18] to simulate spin dynamics and pump−probe Kerr rotation for general solid-state systems. The approach is free from empirical parameters and is thus of great predictive power. Through the complete first-principles descriptions of light−matter interaction and scattering processes including electron−phonon, electron−impurity, and electron−electron scatterings with self-consistent spin−orbit coupling (SOC) and Landé g-factor, our method can predict τ_s as a function of temperature and carrier density, under electric and magnetic fields. The method was applied to disparate materials, including semiconductors and metals, with and without inversion symmetry, in good agreement with experimental results.[16−21]

In this work, we briefly introduce the theory and implementation of our method with brief comparisons to other ab initio methods and then present its applications and show its predictive power using a two-dimensional Dirac material—Germanene—as a showcase. Through detailed theoretical analysis, we show how ab initio simulations improve our understandings of spin relaxation mechanisms and are used to identify the key quantities and/or factors to spin relaxation, dephasing, and diffusion. At the end, we discuss how our FPDM approach can be generalized/extended to simulate spin dynamics of excitons, instead of free carriers, and transport properties such as photocurrent and spin currents in broken inversion systems (photogalvanic effect).

II. THEORY

II.A. Density-Matrix (DM) Master Equation.

II.A.1. Quantum Master Equation. To provide a general formulation of quantum dynamics in solid-state materials, we start from the Liouville−von Neumann equation in the Schrödinger picture,

$$\frac{\mathrm{d}\rho(t)}{\mathrm{d}t} = -\frac{i}{\hbar}[H, \rho(t)] \tag{1}$$

$$H = H_0 + H' \tag{2}$$

where H, H_0, and H' are total, unperturbed, and perturbation Hamiltonians, respectively. In this work,

$$H_0 = H_e + H_{\mathrm{ph}} + H_{\mathrm{photon}} \tag{3}$$

$$H' = H_{\mathrm{e-light}} + H_{\mathrm{e-ph}} + H_{\mathrm{e-i}} + H_{\mathrm{e-e}} \tag{4}$$

where H_e, H_{ph}, and H_{photon} are single-particle electronic, phonon, and photon Hamiltonian, respectively. $H_{\mathrm{e-light}}$ is the light−matter interaction term. $H_{\mathrm{e-ph}}$, $H_{\mathrm{e-i}}$, and $H_{\mathrm{e-e}}$ describe the electron−phonon (e−ph), electron−impurity (e−i), and electron−electron (e−e) interactions, respectively.

In practical simulations of ultrafast dynamics or quantum transport of Bloch electrons, it is more convenient to reduce the many-body density matrix in eq 1 to one-particle density matrix for electrons, where the environmental degree of freedom is traced out,[22] with a proper truncated BBGKY ((Bogolyubov−Born−Green−Kirkwood−Yvon) hierarchy.[23,24] The total rate of change of the electronic DM ρ is separated into terms related to different parts of Hamiltonian,

$$\frac{\mathrm{d}\rho}{\mathrm{d}t} = \left.\frac{\mathrm{d}\rho}{\mathrm{d}t}\right|_{\mathrm{coh}} + \left.\frac{\mathrm{d}\rho}{\mathrm{d}t}\right|_{\mathrm{scatt}} \tag{5}$$

where $\left.\frac{\mathrm{d}\rho}{\mathrm{d}t}\right|_{\mathrm{coh}}$ describes the coherent dynamics of electrons including the free-particle dynamics, the field-induced dynamics, etc. $\left.\frac{\mathrm{d}\rho}{\mathrm{d}t}\right|_{\mathrm{scatt}}$ captures the scattering between electrons and other particles. Their detailed forms are given in the subsections below.

To obtain eq 5, which involves only the dynamics of electrons or the electronic subsystem, we have assumed the environmental subsystem is characterized by a huge number of degrees of freedom and is not perturbed by the electronic subsystem, which implies that the occupations of phonons and photons stay at their equilibrium values at certain temperature, i.e., the "hot phonons" are not considered. Formally this is the prerequisite for the Markov approximation. For spin lifetime simulations, this assumption is valid in following conditions. (i) The correlation time of the environment τ_c is much shorter than the characteristic time scale of spins, which is determined by τ_s and spin precession time $1/\Omega$. This condition is satisfied in most of our theoretical studies where τ_s are long (i.e., ps to μs) and spin precessions are relatively slow. It ensures spin evolves slowly so that the memory effects of the bath (e.g., phonon) can be safely dropped. (ii) The electronic system is not far from initial equilibrium; e.g., the excited carrier density is not very high (correspondingly, the experimental pump power is low). This ensures that the heat received by the environment can quickly decay out. In most spin dynamics experiments, it is desirable to work under the low excitation density limit to focus on the physics of spin dynamics, which is often the slowest, compared to other quasiparticles' dynamics. Indeed in many experiments, e.g., in refs 25. and26, pump fluence and excitation density are controlled to be low, e.g., 2×10^{14} cm^{-3} for a three-dimensional system. If spin lifetime and diffusion length are obtained from spin transport measurement, then it is designated at the (quasi-)equilibrium condition. In fact spin lifetime is quite similar between spin transport and time-resolved Kerr rotation measurements as materials' properties, which again validates the approximations we explained here.

It is true that the Markov approximation fails in certain conditions. For example, if τ_c of the environmental subsystem is comparable to or longer (but not infinite) than τ_s or $1/\Omega$.[8] Or the short-time evolution is the focus, such as hot-carrier

https://doi.org/10.1021/acs.jctc.3c00598
J. Chem. Theory Comput. 2024, 20, 492−512

ultrafast dynamics or photocatalytic processes. The inclusion of dynamics of the environment, e.g., phonon degrees of freedom in the dynamics, or formally non-Markovian effects by taking into account the memory effect of phonon bath, has been discussed in detail in refs 22 and 27. Such development in principles can be built on top of the current numerical implementations; however it is much more computationally costly due to additional dynamics of the bath.

II.A.2. Coherent Terms and External Fields. In general, a coherent term corresponding to a single-particle electronic Hamiltonian H_e reads

$$\left.\frac{d\rho}{dt}\right|_{free} = -\frac{i}{\hbar}[H_e, \rho] \tag{6}$$

where $[H_e,\rho] = H\rho - \rho H$. In absence of external fields, the coherent term is simply the free evolution $\left.\frac{d\rho}{dt}\right|_{free}$ and H_e is the unperturbed electronic Hamiltonian, practically computed at the mean-field level, i.e., from density functional theory (DFT). With the electronic eigenbasis,

$$H_{e,kmn} = \epsilon_{kn}\delta_{mn} \tag{7}$$

where k is the k-point index, m and n are band indices, ϵ is the single-particle energy, and δ_{mn} is the Kronecker delta function.

Therefore, we have

$$\left(\left.\frac{d\rho}{dt}\right|_{free}\right)_{kmn} = -\frac{i}{\hbar}(\epsilon_{km} - \epsilon_{kn})\rho_{kmn} \tag{8}$$

We note that the time-dependent electronic state renormalization due to many-body interactions, e.g., time-dependent electron correlation contribution to one particle density matrix, can be included in the electronic Hamiltonian, which will introduce additional terms in coherent dynamics.[8,28,29]

The state renormalization may cause the following: (i) the effective mass of electrons change; (ii) $\mathbf{k}$-dependent (and time-dependent) effective magnetic fields.[8] The former was extensively studied for various materials,[30,31] and it is of great interest to reexamine such effect on τ_s. In ref 8, it was pointed out that the latter effect presents and can be important to τ_s if highly spin-polarized excited carriers with a high density exist. This is however irrelevant to this work, which focuses on low excitation density. The ab initio studies of this effect within the DM master equation approach are of great interest but are complicated and expensive.

The inclusion of external fields in the DM approach for solid-state materials is not trivial and was studied by many theorists since the 1950s.[32−38] Here, we consider three spatially homogeneous fields as follows.

II.A.2.1. Laser Field. In this work, we approximate that the light-mater interaction $H_{e-light}$ consists of two parts—a semiclassical part H_{laser} describing electrons moving in a laser field (i.e., an electromagnetic field caused by the incident laser) and a quantum part describing the electron−photon interaction in the vacuum without considering the laser. The semiclassical part corresponds to light absorption and stimulated emission under a laser field, while the quantum part corresponds to spontaneous emission. We discuss the coherent term due to the semiclassical part first but discuss the quantum part in the next subsection.

The Hamiltonian of a laser in the velocity gauge with frequency ω_{laser} is approximately[16]

$$H_{laser,kmn}(\omega, t) = \frac{e}{m_e}\mathbf{A}_{laser}(t)\cdot\mathbf{p}_{kmn} + \text{H.C.} \tag{9}$$

where H.C. is the Hermitian conjugate. $\mathbf{A}_{laser}(t)$ is the vector potential. $\mathbf{A}_{laser}(t)$ is real/complex for linearly/circularly polarized light, respectively. $\mathbf{p}_{kmn}$ is the momentum operator matrix element; i.e., $\mathbf{p} = -i/\hbar[\mathbf{r},H_e]$, which includes the contribution of the nonlocal part of the pseudopotentials.

For a Gaussian pump pulse centered at time t_{center} with width τ_{pump},

$$\mathbf{A}_{laser}(t) = \mathbf{A}_{laser} f^G(t)\exp(i\omega_{laser}t) \tag{10}$$

$$f^G(t) = \frac{1}{\sqrt{\sqrt{\pi}\tau_{pump}}}\exp\left[-\frac{(t - t_{center})^2}{2\tau_{pump}^2}\right] \tag{11}$$

Note that the corresponding pump power is $I_{laser} = \omega_{laser}^2|\mathbf{A}_{laser}|^2/(2\pi\alpha)$ (we note that, in ref 16, a factor of 4 is missing for I_{laser}), where α is the fine structure constant.

The corresponding dynamics is

$$\left.\frac{d\rho}{dt}\right|_{laser} = -\frac{i}{\hbar}[H_{laser}, \rho] \tag{12}$$

II.A.2.2. Static Electric Field along a Nonperiodic Direction. Such electric field along the nonperiodic direction E_{np} is directly included in the DFT calculation and is modeled by a ramp or saw-like potential. Under such treatment, H_e is E_{np}-dependent. As all terms of the master equation (eq 5) are built on eigensystems from H_e, they are all E_{np}-dependent. However, if electric field is applied along the periodic direction, one needs to properly treat the periodic boundary condition (e.g., using the modern theory of polarization[39,40]).

II.A.2.3. Magnetic Field. We describe the effects of an external magnetic field $\mathbf{B}^{ext}$ using Zeeman Hamiltonian

$$H_{Z,k}(\mathbf{B}^{ext}) = \mu_B\mathbf{B}^{ext}\cdot(\mathbf{L}_k + g_0\mathbf{S}_k) \tag{13}$$

where μ_B is Bohr magneton; g_0 is the free-electron g-factor; $\mathbf{S}$ and $\mathbf{L}$ are the spin and orbital angular momentum, respectively. The simulation of $\mathbf{L}$ is nontrivial for periodic systems. With the Blöch basis, the orbital angular momentum reads

$$\mathbf{L}_{k,mn} = i\left\langle \frac{\partial u_{km}}{\partial\mathbf{k}}\middle|(\hat{H}_e(\mathbf{B}^{ext}=0) - \bar{\varepsilon}_{kmn})\middle|\frac{\partial u_{kn}}{\partial\mathbf{k}}\right\rangle \tag{14}$$

$$\bar{\varepsilon}_{kmn} = \frac{\varepsilon_{km} + \varepsilon_{kn}}{2} \tag{15}$$

where u is the periodic part of the single-particle wave function; $\hat{H}_e(\mathbf{B}^{ext}=0)$ is the zero-field Hamiltonian operator. Equation 14 can be proven equivalent to $\mathbf{L} = 0.5(\mathbf{r}\times\mathbf{p} - \mathbf{p}\times\mathbf{r})$ with $\mathbf{r}$ being the position operator. The detailed implementation of eq 14 is described in ref 41.

There are two ways to consider magnetic-field effects. The first way is including $H_{Z,k}(\mathbf{B}^{ext})$ in H_e perturbatively (instead of self-consistently); then the new eigensystems can be obtained by diagonalizing $H_e(\mathbf{B}^{ext} \neq 0)$. The second way is including $H_{Z,k}(\mathbf{B}^{ext})$ in H' and the corresponding coherent dynamics is $-\frac{i}{\hbar}[H_{Z,k}(\mathbf{B}^{ext}), \rho]$. In practice, the two approaches lead to nearly the same dynamical quantities such as lifetimes, since $H_{Z,k}(\mathbf{B}^{ext})$ is rather weak—e.g., Zeeman splitting under 1 T is of order 0.1 meV for many solid-state systems. In addition, we

https://doi.org/10.1021/acs.jctc.3c00598
J. Chem. Theory Comput. 2024, 20, 492−512

note that we do not consider the effect of very strong magnetic field such as the appearance of Landau level in this work.

II.A.3. Scattering Terms. Under Born−Markov approximation and neglecting renormalization of single-particle states due to many-body interactions, in general we have[42]

$$\left.\frac{\mathrm{d}\rho_{12}}{\mathrm{d}t}\right|_c = \frac{1}{2}\sum_{345}\begin{bmatrix}(I-\rho)_{13}P_{32,45}\rho_{45}\\ -(I-\rho)_{45}P^*_{45,13}\rho_{32}\end{bmatrix} + \text{H.C.} \tag{16}$$

$$P = \sum_c P^c \tag{17}$$

where P is the generalized scattering-rate matrix. The subindex, e.g., "1", is the combined index of k-point and band. For simplicity, when summing over k-points, the weights of k-points are omitted. c labels a scattering channel corresponding to an interaction Hamiltonian H_c. P_c of several scattering channels are given below.

II.A.3.1. Electron−Phonon. The generalized electron−phonon (e−ph) scattering-rate matrix reads[42]

$$P^{\mathrm{e-ph}}_{1234} = \sum_{q\lambda\pm} A^{q\lambda\pm}_{13}A^{q\lambda\pm,*}_{24} \tag{18}$$

$$A^{q\lambda\pm}_{13} = \sqrt{\frac{2\pi}{\hbar}}\, g^{q\lambda\pm}_{13}\sqrt{\delta^G_\sigma(\omega_{13}\pm\omega_{q\lambda})}\sqrt{n^{\pm}_{q\lambda}} \tag{19}$$

$$\omega_{13} = \epsilon_1 - \epsilon_3 \tag{20}$$

where q is a phonon wavevector. λ is phonon mode. "+" and "−" correspond to the absorption and emission of a phonon, respectively. $g^{q\lambda\pm}$ is the e−ph matrix element. $n^{\pm}_{q\lambda} = n_{q\lambda} + \frac{1}{2} \pm \frac{1}{2}$, with n_q phonon occupation or Bose−Einstein distribution function. δ^G_σ represents an energy conserving δ-function broadened to a Gaussian function of width σ. The explicit derivation of the above $P^{\mathrm{e-ph}}$ can be found in ref 42. This form guarantees the positive definition of single-particle density matrix. $g^{q\lambda\pm}$ is computed fully from first-principles with self-consistent spin−orbit coupling based on density-functional perturbation theory and Wannier interpolation methods.[43]

According to ref 42, there exist two alternative pathways to arrive at the Markov limit of the scattering term, leading to two different forms of $P^{\mathrm{e-ph}}$. One is given above in eq 18 with a symmetric structure (containing square root of two Gaussian functions) and is called the Lindbladian form of $P^{\mathrm{e-ph}}$ here. Another is non-Lindblad, contains a single Dirac delta function, and reads

$$P^{\mathrm{e-ph}}_{1234} = \sum_{q\lambda\pm} a^{q\lambda\pm}_{13}b^{q\lambda\pm,*}_{24} \tag{21}$$

$$a^{q\lambda\pm}_{13} = \frac{1}{\hbar}g^{q\lambda\pm}_{13}\sqrt{n^{\pm}_{q\lambda}} \tag{22}$$

$$b^{q\lambda\pm}_{13} = 2\pi g^{q\lambda\pm}_{13}\sqrt{n^{\pm}_{q\lambda}}\,\delta(\omega_{13}\pm\omega_{q\lambda}) \tag{23}$$

Equation 21 is called the conventional form of $P^{\mathrm{e-ph}}$ here. Such form does not preserve the positive-definite character of the density matrix ρ, unlike the Lindbladian form,[42] although we find that two forms of $P^{\mathrm{e-ph}}$ lead to rather similar τ_s (within 20% for various materials) and the same carrier lifetime τ_p. Therefore, we will stick to the Lindbladian form of $P^{\mathrm{e-ph}}$.

II.A.3.2. Electron−Impurity. Similar to the e−ph scattering, the generalized e−i scattering-rate matrix reads

$$P^{\mathrm{e-i}}_{1234} = A^{i}_{13}A^{i,*}_{24} \tag{24}$$

$$A^{\mathrm{i}}_{13} = \sqrt{\frac{2\pi}{\hbar}}\, g^{\mathrm{i}}_{13}\sqrt{\delta^G_\sigma(\omega_{13})}\sqrt{n_{\mathrm{i}}V_{\mathrm{cell}}} \tag{25}$$

$$g^{\mathrm{i}}_{13} = \langle 1|\Delta V^{\mathrm{i}}|3\rangle \tag{26}$$

$$\Delta V^{\mathrm{i}} = V^{\mathrm{i}} - V^0 \tag{27}$$

where n_{i} and V_{cell} are impurity density and unit cell volume, respectively, V^{i} is the potential of the impurity system, and V^0 is the potential of the pristine system. Here we assume impurities are randomly distributed and impurity density is sufficiently low so that the average distance between neighboring impurities is sufficiently long with nearly no interactions among impurities.

In our implementation, g^{i} of neutral impurities are computed fully from first-principles, where V^{i} is computed using the defect supercell method with SOC.[44] On the other hand, for ionized impurities, we approximate ΔV^{i} as the screened Coulomb potential of a point charge with effective charge Z.[45] Such approximate ΔV^{i} is accurate in the long-range limit;[45] i.e., its Fourier transform $\Delta V^{\mathrm{i}}(q)$ is accurate when $q \to 0$, so that it is most suitable for the intravalley relaxation process due to electron−impurity scatterings. The justification of this approximation is that the long-range part is the most dominant in the electrostatic interaction of ionized impurities.[45]

In addition, for nonmagnetic impurities, the impurity effects can be directly simulated via the coherent dynamics,[46]

$$\left.\frac{\mathrm{d}\rho}{\mathrm{d}t}\right|_{\mathrm{e-i}} = -i[\Delta V^{\mathrm{i}}, \rho] \tag{28}$$

This naturally includes both the damping and renormalization effects of impurities nonperturbatively. Such simple formula is however numerically cumbersome for propagating the quantum master equation in real time. The improvement based on such a formula needs to be studied in future works.

The effects of magnetic impurities on τ_s are essential for diluted magnetic semiconductors, a promising class of spintronic materials, and possibly critical to spin relaxation in graphene.[47] Such effects are complicated, since magnetic impurities exchange spins with electrons and in principle the dynamics of impurity spins/magnetization should be considered. The spin/magnetization fluctuation further complicates spin dynamics of free carriers. According to ref 8, at zero external magnetic field $\mathbf{B}^{\mathrm{ext}} = 0$, the main effect of paramagnetic impurities on spin relaxation of bulk or delocalized carriers is to induce spin−flip transitions through the exchange interaction (expect other parts of ΔV^{i} unrelated to spin exchange), which can be simulated via FGR or T-matrix.[47] For paramagnetic impurities at $\mathbf{B}^{\mathrm{ext}} \neq 0$ or magnetic impurities producing a net magnetization, free carriers will precess about the effective magnetic fields generated by impurities.[8] The magnitude and $\mathbf{k}$-dependence of the effective magnetic fields may affect spin relaxation, dephasing, and diffusion significantly.

II.A.3.3. Electron−Electron Interaction. The generalized e−e scattering-rate matrix reads[42]

https://doi.org/10.1021/acs.jctc.3c00598
J. Chem. Theory Comput. 2024, 20, 492−512

$$P^{e-e}_{1234}=2\sum_{56,78}(I-\rho)_{65}\mathcal{A}_{15,37}\mathcal{A}^{*}_{26,48}\rho_{78} \tag{29}$$

$$\mathcal{A}_{1234}=\frac{1}{2}(A_{1234}-A_{1243}) \tag{30}$$

$$A_{1234}=\frac{1}{2}\sqrt{\frac{2\pi}{\hbar}}[g^{e-e}_{1234}(\delta^{G}_{\sigma,1234})^{1/2}+g^{e-e}_{2143}(\delta^{G}_{\sigma,2143})^{1/2}] \tag{31}$$

$$\delta^{G}_{\sigma,1234}=\delta^{G}_{\sigma}(\epsilon_1+\epsilon_2-\epsilon_3-\epsilon_4) \tag{32}$$

$$g^{e-e}_{1234}=\langle 1(\mathbf{r})|\langle 2(\mathbf{r}')|W(\mathbf{r}-\mathbf{r}')|3(\mathbf{r})\rangle|4(\mathbf{r}')\rangle \tag{33}$$

where $W(\mathbf{r}-\mathbf{r}')$ is the screened Coulomb potential between two electrons at $\mathbf{r}$ and $\mathbf{r}'$. Note that P^{e-e} is ρ-dependent due to the two-particle nature of the e−e scattering and needs to be updated during the time evolution. P^{e-e} can be separated into a direct term ($P^{e-e,d}$) and an exchange term ($P^{e-e,x}$),

$$P^{e-e}=P^{e-e,d}-P^{e-e,x} \tag{34}$$

$$P^{e-e,d}=\sum_{56,78}(I-\rho)_{65}A_{15,37}A^{*}_{26,48}\rho_{78} \tag{35}$$

$$P^{e-e,x}=\sum_{56,78}(I-\rho)_{65}A_{15,37}A^{*}_{26,84}\rho_{78} \tag{36}$$

According to ref 22, since the direct term is expected to dominate the scattering processes among electrons or holes, the exchange term is neglected here.

In our current implementation, the static random phase approximation (RPA) dielectric function is used for dielectric screening without local-field effects.[16] Future studies of the effect of dynamic screening and local field would be beneficial.

II.A.3.4. Spontaneous Emission. As discussed above, in this work, the light−matter interaction consists of a semiclassical part (absorption and simulated emission by a laser field) and a quantum part. The semiclassical part has been discussed above (Section II.A.2). Here we discuss the quantum part, which describes the electron−photon interaction in the vacuum. Similar to the electron−phonon scattering, we write a similar form for electron−photon interaction (the underlying consideration on positive definition of density matrix is similar).[42]

$$P^{sp-em}_{1234}=\sum_{q\lambda\pm}A^{photon,q\lambda\pm}_{13}A^{photon,q\lambda\pm,*}_{24} \tag{37}$$

$$A^{photon,q\lambda\pm}_{13}=\sqrt{\frac{2\pi}{\hbar}}g^{photon,q\lambda\pm}_{13}\sqrt{\delta^{G}_{\sigma}(\omega_{13}\pm\omega^{photon}_{q\lambda})} \tag{38}$$

$$\times\sqrt{n^{photon,\pm}_{q\lambda}} \tag{39}$$

where " + " and "−" correspond to photon emission and absorption, respectively; λ is the photon mode; and $g^{photon,q\lambda\pm}_{13}$ is the electron−photon matrix element proportional to $\mathbf{p}$ matrix element. The differences from P^{e-ph} are as follows: (i) As ω^{photon} is comparable to the band gap which is much greater than k_BT, $n^{photon,-}_{q\lambda}\approx 0$ and $n^{photon,+}_{q\lambda}\approx 1$. This represents that photon absorption is not allowed in vacuum and every photon emission process emits one photon. (ii) As photon momentum q is tiny (at long wavelength limit), for A^{photon}_{13}, we have $\mathbf{k}_1\approx\mathbf{k}_3$. Therefore,

$$A^{photon,q\lambda+}_{13}=\sqrt{\frac{2\pi}{\hbar}}g^{photon,q\lambda+}_{13}\sqrt{\delta^{G}_{\sigma}(\omega_{13}+\omega^{photon}_{q\lambda})}\,\delta_{\mathbf{k}_1\mathbf{k}_3} \tag{40}$$

The detailed form of P^{sp-em}_{1234} will be given in our future work.

II.A.4. Linearized Quantum Master Equation. If the system is weakly perturbed from its equilibrium, e.g., by a small magnetic field or a weak pump pulse, the density matrix can be written as

$$\rho=\rho^{eq}+\delta\rho \tag{41}$$

where $\rho^{eq}\equiv f^{eq}$ is the Fermi−Dirac distribution function. Neglecting the second-order terms (in terms of $\delta\rho$), with the coherent and scattering terms given above, the DM master equation reads as

$$\frac{d(\delta\rho)}{dt}=-\frac{i}{\hbar}[H_e,f^{eq}]-\frac{i}{\hbar}[H_e,\delta\rho]+\frac{d(\delta\rho)}{dt}\Big|^{lin,I}_{scatt}+\frac{d(\delta\rho)}{dt}\Big|^{lin,II}_{scatt} \tag{42}$$

$$\left(\frac{d(\delta\rho)}{dt}\Big|^{lin,I}_{scatt}\right)_{12}=\frac{1}{2}\sum_{ab}\tilde{P}_{12,ab}[f^{eq}]\delta\rho_{ab}+\text{H.C.} \tag{43}$$

$$\tilde{P}_{12,ab}[f^{eq}]=\begin{bmatrix}(1-f^{eq}_1)P^{(0)}_{12,ab}\\ -\delta_{1b}\sum_3 P^{(0)}_{b2,33}f^{eq}_3\\ -\sum_3(1-f^{eq}_3)P^{(0),*}_{33,1a}\delta_{2b}\\ +P^{(0),*}_{ab,12}f^{eq}_2\end{bmatrix} \tag{44}$$

$$\left(\frac{d(\delta\rho)}{dt}\Big|^{lin,II}_{scatt}\right)_{12}=\frac{1}{2}\sum_3\begin{bmatrix}(1-f^{eq}_1)P^{(1)}_{12,33}f^{eq}_3\\ -(1-f^{eq}_3)P^{(1),*}_{33,12}f^{eq}_2\end{bmatrix}+\text{H.C.} \tag{45}$$

where $P^{(0)}$ and $P^{(1)}$ are the zero- and first-order parts (in terms of $\delta\rho$) of P, respectively. Since P^{e-e} is ρ-dependent, $P^{e-e,(1)}$ is nonzero and is found to be critical to both carrier and spin dynamics/transport. On the other hand, P^{e-ph} and P^{sp-em} are ρ-independent, so that $P^{e-ph,(1)}\equiv P^{sp-em,(1)}\equiv 0$. For ionized impurities, P^{e-i} depends on ρ indirectly due to the carrier-density-dependence of the screening. This indirect ρ-dependence of P^{e-i} is found to be unimportant when $\delta\rho$ is tiny and is always neglected, so that $P^{e-i,(1)}$ is taken to 0.

To derive the above equations, we have used the relation $\frac{df^{eq}}{dt}\Big|_{scatt}=0$, which is true since the scattering should be absent at equilibrium if we omit the energy renormalization effects of the scattering.

When H_e is band-diagonal; i.e., $H_{e,kmn}=\epsilon_{km}\delta_{mn}$, and $[H_e f^{eq}]\equiv 0$. In such cases, only the first-order terms of the linearized master equation (eq 42) are nonzeros. Thus, eq 42 can be rewritten as

$$\frac{d(\delta\rho)_{12}}{dt}=\sum_{ab}L^{LME}_{12,ab}\delta\rho_{ab} \tag{46}$$

https://doi.org/10.1021/acs.jctc.3c00598
J. Chem. Theory Comput. 2024, 20, 492−512

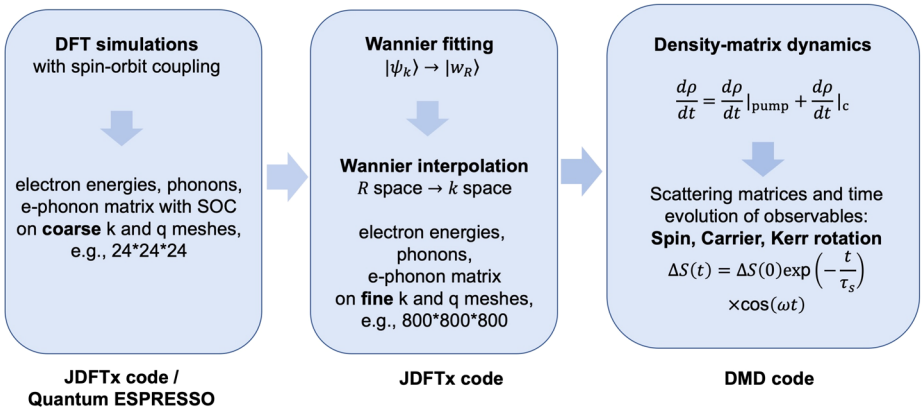

Figure 1. Work flow of a spin dynamics simulation. The codes implemented for different steps are listed and explained in the main text.

The detailed form of $L^{\text{LME}}_{12,ab}$ will be given in our future work. When the system is close to the equilibrium, the linearized master equation is numerically preferred (faster and more accurate), especially for the e−e scattering. Moreover, the simpler mathematical form of eq 46 potentially allows us to solve the DM master equation using more elegant numerical methods.

II.B. Spin Lifetime and Spin Diffusion Length.

II.B.1. Spin Lifetime: Relaxation and Dephasing. In most spin lifetime τ_s experiments, τ_s of ensemble spins are measured. The spin observable of an ensemble is

$$S_i^{\text{tot}}(t)=\text{Tr}[s_i\rho(t)] = \sum_k \sum_{mn} s_{i,kmn}\rho_{knm}(t) \tag{47}$$

where s_i is a spin Pauli matrix in Blöch basis along direction i. For spin dynamics, the total excited or excess spin observable is often more relevant and is defined as

$$S_i^{\text{ex}}(t) = S_i^{\text{tot}}(t) - S_i^{\text{eq}}(t) \tag{48}$$

where "eq" denotes equilibrium.

An ultrafast simulation of $\tau_{s,i}$ starts at an initial state (at $t = t_0$) with $\delta\rho(t_0) = \rho(t_0) - \rho^{\text{eq}} \neq 0$, which leads to a net spin $S_i^{\text{ex}}(t) \neq 0$. We evolve $\rho(t)$ through the quantum master eq eq 5 for a long enough simulation time, typically from a few ps to a few hundred ns, until the evolution of $S_i^{\text{ex}}(t)$ can be reliably fitted by

$$S_i^{\text{ex}}(t) = S_i^{\text{ex}}(t_0)\exp\left[-\frac{t-t_0}{\tau_{s,i}}\right] \tag{49}$$

$$\times \cos[\omega(t-t_0)+\phi] \tag{50}$$

to extract the relaxation time, $\tau_{s,i}$. Above, ω is oscillation frequency due to Larmor precession.

In ref 16, we have shown that one can generate the initial spin imbalance by applying a test magnetic field at $t = -\infty$, allowing the system to equilibrate with a net spin and then turning it off suddenly at t_0, in order to measure spin relaxation.

Historically, spin relaxation time (or longitudinal time) T_1 and ensemble spin dephasing time (or transverse time) T_2^* were used to characterize the decay of spin ensemble.[8,48] Suppose the spins of the system are polarized along direction $\mathbf{r}_0$, possibly due to applying a constant external field $\mathbf{B}_0$ along $\mathbf{r}_0$, and suppose the total excess/excited spin is along direction $\mathbf{r}_1$, if $\mathbf{r}_1 \| \mathbf{r}_0$ (or $\mathbf{r}_1 \perp \mathbf{r}_0$), τ_s is called T_1 (or T_2^*). For T_2^*, the excess spin $\mathbf{S}^{\text{ex}}(t)$ precesses with a frequency proportional to $|\mathbf{B}_0|$.

The ensemble spin dephasing rate $1/T_2^*$ consists of reversible part and irreversible part. The reversible part may be removed by the spin echo technique. The irreversible part is called spin dephasing rate $1/T_2$, which must be smaller than $1/T_2^*$. According to ref 48, T_2 may be also defined using eq 50 without the need of spin−echo but instead of $S_i^{\text{tot}}(t)$, we need another quantity—the sum of individual spin amplitudes

$$S_i^{\text{indiv}} = \sum_k \sum_{mn} |s_{i,kmn}\rho_{knm}(t)| \tag{51}$$

II.B.2. Optical Measurements. Ultrafast magneto-optical pump−probe measurements such as time-resolved Kerr/Faraday rotation (TRKR/TRFR) are powerful tools for studying the dynamics of spin or magnetic polarization and are thus widely used to measure τ_s.[25,49−51] In these ultrafast measurements, a circularly polarized pump pulse (Section II.A.2.1 "Laser Field") is first used to excite the electron spins and hole spins via the optical transitions, which approximately induce a change of the secondary total angular momentum $\Delta m_j = \pm 1$ for left and right circular polarization, respectively. The evolution of the total spin polarization is detected by many repeated weak "probe" pulses. For example, in TRKR (TRFR) experiments, the linearly polarized probe pulses are reflected by (transmitted through) the material and the rotations of their polarization planes at different time are detected. The dynamics of the rotation approximately follows the dynamics of the total spin polarization, which was confirmed by the theoretical simulations in ref 16.

In general, the optical signal including the Kerr/Faraday rotation angle can be simulated from the density-matrix change induced by a probe pulse—$\Delta\rho^{\text{probe}}$. The probe pulse interacts with the material the same as the pump pulse, except that the probe−pulse density is typically low. Therefore, within the second-order time-dependent perturbation theory, we have

$$\Delta\rho^{\text{probe}} = \frac{1}{2}\sum_{345}\left\{\begin{array}{l}[I-\rho(t)]_{13}P^{\text{probe}}_{32,45}\rho(t)_{45} \\ -[I-\rho(t)]_{45}P^{\text{probe}}_{45,13}\rho(t)_{32}\end{array}\right\} + \text{H.C.} \tag{52}$$

$$P^{\text{probe}}_{1234} = \sum_{\pm} A^{\text{probe},\pm}_{13}A^{\text{probe},\pm,*}_{24} \tag{53}$$

https://doi.org/10.1021/acs.jctc.3c00598
J. Chem. Theory Comput. 2024, 20, 492−512

$$A_{13}^{\text{probe},\pm} = \sqrt{\frac{2\pi}{\hbar}}\frac{e}{m_e}(\mathbf{A}^{\text{probe}}\cdot\mathbf{p})\sqrt{\delta_\sigma^{\text{G}}(\omega_{13} \pm \omega^{\text{probe}})} \tag{54}$$

With $\Delta\rho^{\text{probe}}$, the dielectric function of the excited state detected by a probe pulse, which is ε, at the independent-particle level, is

$$\text{Im}\ \varepsilon = \text{Im}\ \varepsilon^{\text{gs}} + \frac{2\pi}{(\omega^{\text{probe}})^3|\mathbf{A}^{\text{probe}}|^2}\text{Tr}(H_e\Delta\rho^{\text{probe}}) \tag{55}$$

With Im ε, the real part Re ε is obtained from the Krames−Kronig relation; ε^{gs} denotes a ground-state dielectric function. Note that Im $\Delta\varepsilon$ is independent of $\mathbf{A}^{\text{probe}}$ as $\Delta\rho^{\text{probe}} \propto |\mathbf{A}^{\text{probe}}|^2$. Moreover, the Im $\Delta\varepsilon$ above is a functional of ρ instead that of the occupation function f in the usual expression of the independent-particle dielectric function.[52]

In TRKR and TRFR, the probe pulse is a linearly polarized one and can be regarded as a superposition of left and right circularly polarized pulses. Define the excited-state dielectric function detected by a left (right) circularly polarized pulse as ε_+ (ε_-), the Kerr rotation angle θ_K is[53]

$$\theta_K = \text{Im}\left(\frac{\sqrt{\varepsilon_+} - \sqrt{\varepsilon_-}}{1-\sqrt{\varepsilon_+}\sqrt{\varepsilon_-}}\right) \tag{56}$$

Similarly, the Faraday rotation can also be obtained from $\varepsilon_\pm$.[53]

II.B.3. Work Flow of a Spin Dynamics Simulation. As shown in Figure 1, a spin dynamics simulation has three main steps:

(i) **DFT step.** The ground-state electronic structure, phonons, as well as the e−ph and e−i matrix elements are first calculated using density functional theory (DFT) with relatively coarse k and q meshes in the DFT plane-wave code JDFTx.[54] The phonon calculation uses the finite difference method with supercells. Alternatively, we can compute the same quantities in QuantumEspresso, with phonon and e−ph couplings calculated by DFPT at the coarse mesh as well.

(ii) **Wannier step.** All quantities in DFT eigenbasis obtained in DFT step are transformed to those in maximally localized Wannier function basis,[55] and then interpolated[43,56−60] to substantially finer k and q meshes. The Wannier interpolation approach fully accounts for long-range dipolar e−ph matrix elements and dipolar correction on phonon dispersion (mainly LO−TO splitting) using the approaches of refs 61 and62 for the 3D and 2D systems. This part is performed in JDFTx code.

(iii) **Dynamics step.** Starting from an initial state with a spin imbalance or with a short circularly polarized pump pulse, we evolve $\rho(t)$ through the quantum master equation of eq 5. After obtaining spin observable $S(t)$ from $\rho(t)$ (eq 47) and fitting $S(t)$ to an exponentially oscillating decay curve (eq 50), the decay constant τ_s is obtained. This part is performed in the DMD code interfacing with the JDFTx code.

II.B.4. Carrier Lifetime and Spin Diffusion Length.
II.B.4.1. Semiclassical Limit and Carrier Lifetime. At the semiclassical limit, ρ is replaced by (non-equilibrium) occupation f, and then the quantum form of the scattering term eq 16 reduces to[16]

$$\left.\frac{df_1}{dt}\right|_c = \sum_{2\neq 1}[(1-f_1)P_{11,22}^c f_2 - (1-f_2)P_{22,11}^c f_1] \tag{57}$$

using the facts that $P_{11,22}$ is real and "2 = 1" term is zero. "c" represent a scattering channel.

The above equation can be linearized as the linearized quantum master equation eq 42,

$$\left.\frac{df_1}{dt}\right|_c = -\sum_{2\neq 1}[P_{11,22}^c f_2^{\text{eq}} + (1-f_2^{\text{eq}})P_{22,11}^c]\delta f_1 \tag{58}$$

using the fact that $P_{11,22}^{(1)} \equiv 0$, even for the e−e scattering.

Define carrier/particle lifetime of state "1" $\tau_{p,1}^c$ by $\left.\frac{df_1}{dt}\right|_c = -\frac{\delta f_1}{\tau_{p,1}^c}$, we have

$$\frac{1}{\tau_{p,1}^c} = \sum_{2\neq 1}[P_{11,22}^c f_2^{\text{eq}} + (1-f_2^{\text{eq}})P_{22,11}^c] \tag{59}$$

The line width or the imaginary part of self-energy is simply Im $\Sigma_1^c = \hbar/(2\tau_{p,1}^c)$.

II.B.4.2. Spin Diffusion Length. The DM approach has been widely employed to simulate transport properties[32,63,64] including spin diffusion length l_s.[8] In principle, the DM master equation approach can be directly applied to simulate quantum diffusion if the off-diagonal elements between different $\mathbf{k}$ are considered.[65] It is however more convenient to simulate transport properties by explicitly including the real-space coordinates in the master equation. This is achieved through the Wigner transformation which constructs the Wigner function $\rho(\mathbf{k},\mathbf{R})$ from the density matrix $\rho(\mathbf{k},\mathbf{k}')$.[66] This approach can be numerically advantageous compared to the fully nonlocal $\mathbf{k}$ space form, where the real-space coordinate can be coarse-grained with a macroscopic scale (tenths of nanometer sizes), while keeping $\mathbf{k}$ sampling still at the microscopic unit-cell level. With the Wigner function master equation, quantum transport simulations (including the l_s simulation) of solid-state materials or devices with arbitrary geometries can be carried out, which allows the direct comparisons to transport measurements such as Hanle-effect measurements of l_s. The first-principles implementation of such an approach is still under development.

In this work, l_s are obtained from first-principles using the commonly used relation[7,8] based on the drift−diffusion model,

$$l_s = \sqrt{D\tau_s} \tag{60}$$

$$D = -\mu_c n_c / \frac{dn_c}{d\epsilon_{\mu_F}} \tag{61}$$

where D is the diffusion coefficient of carriers calculated using the generalized Einstein relation.[67] The underlying assumption here is the diffusion coefficient of carrier being the same as spin, which was shown to be true in graphene-derived systems experimentally.[68] ϵ_{μ_F} is the electron chemical potential. n_c is the carrier density. μ_c is the carrier mobility calculated by solving the linearized Boltzmann equation in momentum−relaxation−time approximation,[69−71]

$$\mu_{c,i} = \frac{e}{n_c V_u}\sum_1 [f^{\text{eq}}]'_1 v_{1,i}{}^2 \tau_{m,1} \tag{62}$$

where $i = x, y, z$. V_u is the unit cell volume. $[f^{\text{eq}}]'$ is the derivative of f^{eq}. v is the band velocity. τ_m is the momentum relaxation time and is approximated as[69−71]

$$\tau_{m,1}{}^{-1} = \sum_{2\neq 1}\{[P_{11,22}f_2^{\text{eq}} + (1-f_2^{\text{eq}})P_{22,11}]\cos\theta_{12}\} \tag{63}$$

https://doi.org/10.1021/acs.jctc.3c00598
J. Chem. Theory Comput. 2024, 20, 492−512

$$\cos\theta_{12} = \frac{\mathbf{v}_1\cdot\mathbf{v}_2}{v_1 v_2} \tag{64}$$

where $\mathbf{v}$ is the velocity vector. We find that τ_m is similar to the carrier lifetime τ_p except the angle factor $\cos\theta_{12}$.

II.C. Comparisons with Other Ab Initio Methods for Spin Dynamics. *II.C.1. Ab Initio NEGF within the KBE.* Within the KBEs (Keldysh−Kadanoff−Baym equations) at equal time arguments ($t = t'$), the equations of motion for one-particle NEGF (non-equilibrium Green's function) approach within Martin−Schwinger (MS) hierarchy can be reduced to the BBGKY hierarchy for the reduced density operators.[28,72,73] The latter approach is the focus of this review. An ab initio implementation of the real-time NEGF approach has been performed by Marini and co-workers to simulate valley depolarization (closely related to spin) in transition metal dichalcogenides (TMDs).[28,52] The time-dependent electron correlation has been included by the Coulomb-hole plus screened-exchange (COHSEX) self-energy through coherent dynamics, which can capture the electron−hole interactions. A similar approach such as time-dependent GW formalism was developed to simulate other time-dependent phenomena such as shift current in broken-inversion symmetry systems.[74] Although the theoretical formalism is general for describing a time-dependent non-equilibrium electronic process, in practice, the scattering dynamics are approximated, i.e., in a form of

$$(\dot{\rho}|_{\text{scatt}})_{kmn} = -\{[(\tau_p^{-1})_{km} + (\tau_p^{-1})_{kn}]/2\}(\rho - \rho^{\text{eq}})_{kmn}$$

The approximations involved in such a form have been detailed in the Supporting Information of ref 52. Such simplification is reasonable for carrier dynamics but may not be justified for spin dynamics, due to the nondiagonal form of density matrix after spin−orbit coupling.

II.C.2. rt-TDDFT. Real-time time-dependent DFT (rt-TDDFT) was developed to simulate ultrafast demagnetization of magnetic systems.[12−14] The basic equation is the time-dependent Kohn−Sham equation

$$i\frac{\partial}{\partial t}\Psi_{kn}(\mathbf{r}, t) = H(\mathbf{r}, t)\,\Psi_{kn}(\mathbf{r}, t) \tag{65}$$

where the time-dependent wave function $\Psi_{kn}(\mathbf{r},t)$ is usually expanded by ground-state Kohn−Sham eigenstates with time-dependent coefficients. The Hamiltonian $H(\mathbf{r},t)$ contains the kinetic term, ionic potential, Hartree potential, a time-dependent vector potential for external laser field, and exchange−correlation (XC) potential $V_{\text{xc}}(\mathbf{r},t)$. The e−e interaction is described through time-dependent V_{xc}. For spin dynamics, two additional terms are needed: one is a time-dependent spin−orbit potential; another term is $\sigma\cdot\mathbf{B}_s(\mathbf{r}, t)$, where $\mathbf{B}_s$ is the KS effective magnetic field including $\mathbf{B}^{\text{ext}}$ and XC magnetic field.[75] The importance of memory effect and accurate electron correlation in rt-TDDFT was investigated through spin−flip TDDFT and dynamical mean-field theory recently.[13]

The e−ph interaction in rt-TDDFT has been described by several different approaches, such as Enrenfest dynamics or surface hopping. The most commonly used Ehrenfest dynamics is a mean-field classical description for nuclear movement, taking into account all electronic excitation at a given time. Such description is good when the effect of nuclear movements is not important or a single trajectory dominates nonadiabatic evolution. Meanwhile, a large supercell is required to simulate the e−ph interactions, in particular for small-q phonon contribution, which leads to extremely high computational cost. Therefore, rt-TDDFT are often aimed at describing the early stages of the demagnetization process (tens to a few hundred fs), when other relaxation mechanisms (e.g., e−ph) can be ignored or are unimportant.

II.C.3. Method Based on Spin−Spin Correlation Function. In ref 15, a method based on spin−spin correlation was developed to simulate spin−phonon relaxation. The formulas are derived using the diagrammatic approach for the phonon-dressed spin vertex. This method avoids real-time propagation which may be computationally convenient. If the system is near equilibrium and only the e−ph interaction is considered, this approach is rather similar to our FPDM approach, because both include only the lowest-order perturbation contribution of the e−ph interaction and have not considered the dynamics of the phonon environment (i.e., Markov approximation). Indeed, their obtained T_1 of Si, WSe_2, and GaAs are rather similar to our FPDM results, when only the e−ph scattering is considered.

On the other hand, our FPDM approach can be generalized straightforwardly to far-from-equilibrium dynamics, when the dynamics of the phonon bath is included. This is rather difficult to do with the approach in ref 15. Moreover, it is not clear how T_2^* can be simulated in their method, especially in the limit where the scattering is absent so that the phonon-dressed spin vertex becomes not meaningful, and inhomogeneous broadening or dephasing process dominates.

II.C.4. Methods Simulating Spin Diffusion Length. Besides the approach based on quantum master equation of the Wigner function $\rho(\mathbf{k},\mathbf{R})$ as mentioned in Section II.B.4, other approaches, such as semiclassical Boltzmann transport equation,[76] non-equilibrium Green's function,[77] Landauer−Büttiker formula,[78] and scattering theory with wave function matching,[79] were widely applied in quantum transport simulations. However, the ab initio approaches for simulating l_s are rare. To the best of our knowledge, fully ab initio simulations of spin diffusion have only been carried out recently for transition metal elements,[79] metallic interfaces,[80] disordered graphene nanoribbons,[81] and double-walled carbon nanotubes.[82] In their ab initio approaches, phonons are either missing or considered through random atomic movements with a given mean-square displacement, so that quantum treatment of the e−ph interaction is difficult. This difficulty can be easily removed from the Wigner function approach.

III. SPIN RELAXATION MECHANISM AND ANALYSIS METHODS FOR SPIN RELAXATION

Through studying the relations between τ_s and important electronic quantities, switching on/off certain dynamic processes, or tuning the key factors affecting spin dynamics, our FPDM method is a powerful technique to determine spin relaxation mechanism and quantitatively predict spin lifetime in different materials at various conditions.

There are several mechanisms causing spin relaxation and dephasing of electron carriers in nonmagnetic systems.[7,8] Among them, the most important mechanisms are Elliot−Yafet (EY) and Dyakonov−Perel (DP) mechanisms. EY represents spin relaxation due to spin−flip scattering. DP is activated when inversion symmetry is broken, which results in random spin precession between adjacent scattering events. Similar to DP mechanism, free induction decay (FID) mechanism is caused by random spin precession but happens when scattering is weak enough. Below we show how to determine

https://doi.org/10.1021/acs.jctc.3c00598
J. Chem. Theory Comput. 2024, 20, 492−512

spin relaxation mechanism and analyze spin relaxation through ab initio simulations. We note that our FPDM approach provides unified treatment for different mechanisms. We also acknowledge that some approximate models were proposed in the past specific for each mechanism, which was helpful for providing mechanistic insights and qualitative understanding. We will introduce them in the following sections. By comparing FPDM and these approximate models, we can further grasp the detailed physical picture of spin relaxation.

III.A. Spin Expectation Value, Spin Texture, and Internal Magnetic Field. We first define some important spin-related properties in spin dynamics.

The diagonal element of spin matrix s_i is named as the spin expectation value $S_i^{\rm exp}$; i.e.,

$$S_{i,1}^{\rm exp} = s_{i,11} \tag{66}$$

Note that for degenerate bands, the matrix elements of s_i are arbitrary; thus, we need to diagonalize s_i matrix in degenerate subspaces.

The spin texture presents when the spin-up and -down degeneracy (Kramers pair) is lifted (e.g., due to broken inversion symmetry) and is the distribution of the spin expectation value vector $\mathbf{S}^{\rm exp} \equiv (S_x^{\rm exp}, S_y^{\rm exp}, S_z^{\rm exp})$.

When there is time-reversal symmetry, if a pair of bands are relatively away from other bands and degenerate without SOC, the main effect of inversion symmetry broken on the pair can be understood as lifting the degeneracy and inducing $\mathbf{k}$-dependent effective SOC fields, called internal magnetic fields $\mathbf{B}_k^{\rm in}$, which split the degenerate pair and polarize the spins along their directions. $\mathbf{B}_k^{\rm in}$ is defined as

$$\mathbf{B}_k^{\rm in} \equiv 2\Delta_k \hat{\mathbf{S}}_k^{\rm exp}/(\mu_B g_0) \tag{67}$$

where Δ is the band splitting energy between a Kramers' degenerate pair before applying SOC. $\hat{\mathbf{S}}_k^{\rm exp} \equiv \mathbf{S}^{\rm exp}/|\mathbf{S}^{\rm exp}|$. From eq 67, $\mathbf{S}_k^{\rm exp} \| \mathbf{B}_k^{\rm in}$ (internal magnetic field $\mathbf{B}_k^{\rm in}$ is along the spin texture direction $\mathbf{S}_k^{\rm exp}$).

III.B. Elliot−Yafet (EY) Mechanism. EY mechanism dominates spin relaxation when spin-up and spin-down are well-defined (in the absence of spin precession), so that it dominates in two types of systems: (i) materials with both time-reversal and spatial inversion symmetries, e.g., silicon, freestanding graphene in the absence of external fields (with such symmetries, every two bands are Kramers degenerate;[7] therefore, spin-up/-down is well-defined along an axis $\hat{\mathbf{r}}$ by diagonalizing the corresponding spin matrix $s_{\mathbf{r}} = \mathbf{s}\cdot\hat{\mathbf{r}}$ in degenerate subspaces); (ii) systems with high spin polarization, e.g., due to spin−valley locking or intrinsic magnetization, e.g., TMDs and ferromagnets.

III.B.1. Fermi's Golden Rule (FGR). III.B.1.1. FGR with Spin−Flip Transitions. For the EY mechanism due to the e−ph scattering, the free carriers' τ_s approximately satisfies[17]

$$\tau_s^{-1} \propto \frac{N_k^{-2}}{\chi} \sum_{kq\lambda} \begin{Bmatrix} |g_{k,k-q}^{\uparrow\downarrow,q\lambda}|^2 n_{q\lambda} f_{k-q}^{\rm eq}(1-f_k^{\rm eq}) \\ \delta(\epsilon_k - \epsilon_{k-q} - \omega_{q\lambda}) \end{Bmatrix} \tag{68}$$

$$\chi = N_k^{-1} \sum_k f_k^{\rm eq}(1-f_k^{\rm eq}) \tag{69}$$

where $g^{\uparrow\downarrow}$ is the spin−flip e−ph matrix element between a spin-up and spin-down state.

According to ref 17, it is helpful to further approximate eqs 68 and 69 into a simple form for analyzing EY-type τ_s^{-1},

$$\tau_s^{-1} \propto \overline{|\tilde{g}^{\uparrow\downarrow}|^2}\, D^{\rm S} \tag{70}$$

where $\overline{|\tilde{g}^{\uparrow\downarrow}|^2}$ is the effective modulus square of the spin−flip e−ph matrix elements and $D^{\rm S}$ is called the scattering density of electronic states (DOS). Both $\overline{|\tilde{g}^{\uparrow\downarrow}|^2}$ and $D^{\rm S}$ depend on T and chemical potential ϵ_{μ_F}, and their detailed formulas are

$$\overline{|\tilde{g}^{\uparrow\downarrow}|^2} = \frac{\sum_{kq} w_{k,k-q} \sum_\lambda |g_{k,k-q}^{\uparrow\downarrow,q\lambda}|^2 n_{q\lambda}}{\sum_{kq} w_{k,k-q}} \tag{71}$$

$$D^{\rm S} = \frac{N_k^{-2} \sum_{kq} w_{k,k-q}}{N_k^{-1} \sum_k f_k^{\rm eq}(1-f_k^{\rm eq})} \tag{72}$$

$$w_{k,k-q} = f_{k-q}^{\rm eq}(1-f_k^{\rm eq})\delta(\epsilon_k - \epsilon_{k-q} - \omega_c) \tag{73}$$

where ω_c is the characteristic phonon energy chosen as the averaged energy of the phonons contributing to spin relaxation and $w_{k,k-q}$ is the weight function.

Therefore, $\overline{|\tilde{g}^{\uparrow\downarrow}|^2}$ selects spin−flip e−ph transitions "more relevant" to spin relaxation or meeting the following three conditions: (i) $n_{q\lambda}$ is non-negligible so that at low T the unoccupied high-frequency phonons do not contribute; (ii) the energy conservation is satisfied; (iii) the electronic states are close to ϵ_{μ_F} or the band edges (otherwise $w_{k,k-q}$ is negligible). $D^{\rm S}$ can be regarded as an effective density of spin−flip e−ph transitions satisfying energy conservation between states close to ϵ_{μ_F} or the band edges.

We can similarly define an effective spin conserving matrix element $\overline{|\tilde{g}^{\uparrow\uparrow}|^2}$ by replacing $g_{k,k-q}^{\uparrow\downarrow,q\lambda}$ to $g_{k,k-q}^{\uparrow\uparrow,q\lambda}$ in eq 71. Then we have the approximate relation for carrier relaxation rate due to e−ph scattering,

$$\langle \tau_p^{-1} \rangle \propto \overline{|\tilde{g}^{\uparrow\uparrow}|^2}\, D^{\rm S} \tag{74}$$

Although such formulas are not as general and accurate as our FPDM formulation, eqs 70 and 74 can be used to understand the spin−flip and spin conserving e−ph matrix element's relation to spin or carrier relaxation and one can develop intuition on what type of phonons contribute more to $\overline{|\tilde{g}^{\uparrow\uparrow}|^2}$ or $\overline{|\tilde{g}^{\uparrow\downarrow}|^2}$. As our recent studies show Fröhlich LO phonon strongly contributes to carrier relaxation in $CsPbBr_3$, but much less important in its spin relaxation due to the spin-conserving nature of long-ranged Fröhlich electron−phonon coupling.[18]

III.B.1.2. Generalized FGR. In centrosymmetric systems with strong spin-mixing and band degeneracy, $\mathbf{S}_k^{\rm exp}$ may have multiple values. For example, valence bands of silicon at Γ are 4-fold degenerate and their $\mathbf{S}_k^{\rm exp}$ are (more precisely, very close to) $\pm 1/2$ and $\pm 1/6$. In such cases, spin relaxation may be still driven by EY mechanism but needs a generalized FGR formula[17] beyond spin−flip transition,

$$\tau_{s,i}^{-1} \propto \frac{N_k^{-2}}{\chi_i} \sum_{12\lambda} \begin{Bmatrix} |\Delta S_{i,12}^{\rm exp} g_{12}^{q,\lambda}|^2 n_{q\lambda} \\ f_2^{\rm eq}(1-f_1^{\rm eq})\delta(\epsilon_1 - \epsilon_2 - \omega_{q\lambda}) \end{Bmatrix} \tag{75}$$

https://doi.org/10.1021/acs.jctc.3c00598
J. Chem. Theory Comput. 2024, 20, 492−512

$$\chi_i = N_k^{-1}\sum_1 f_1^{eq}(1-f_1^{eq})S_{i,1}^{exp,2} \tag{76}$$

$$\Delta S_{i,12}^{exp} = S_{i,1}^{exp} - S_{i,2}^{exp} \tag{77}$$

Therefore, the transitions with non-negligible ΔS^{exp} can contribute to spin relaxation. Again, unlike our FPDM method, this is an approximate formula, which can be used to understand how e−ph scattering between a pair of states changes the spin expectation value as we showcase bulk Si hole spin relaxation in ref 17.

III.B.2. Spin-Mixing Parameter b^2. III.B.2.1. State-Resolved b^2. Suppose the spin of a state "1" is highly polarized along the i direction. Then in general, the wave function of state "1" can be written as $\Psi_1(\mathbf{r}) = a_{i,1}(\mathbf{r})\alpha + b_{i,1}(\mathbf{r})\beta$, where a and b are the coefficients of the large and small spin components and α, β = ↑, ↓ are spinors (along i direction). Define ${a_{i,1}}^2 = \int |a_{i,1}(\mathbf{r})|^2 d\mathbf{r}$ and ${b_{i,1}}^2 = \int |b_{i,1}(\mathbf{r})|^2 d\mathbf{r}$ with $a_{i,1}^2 > b_{i,1}^2$, then $b_{i,1}^2$ is just a spin-mixing parameter of state "1" along direction i.[19]

$${a_{i,1}}^2 + {b_{i,1}}^2 = 1 \tag{78}$$

$$0.5({a_{i,1}}^2 - {b_{i,1}}^2) = S_{i,1}^{exp} \tag{79}$$

Therefore,

$${b_{i,1}}^2 = 0.5 - S_{i,1}^{exp} \tag{80}$$

III.B.2.2. EY Relation. According to eqs 68 and 74, we have

$$\tau_s^{-1}/\tau_p^{-1} \propto \overline{|\tilde{g}^{\uparrow\downarrow}|^2}/\overline{|\tilde{g}^{\uparrow\uparrow}|^2} \tag{81}$$

where $\tau_p = 1/\langle {\tau_p}^{-1}\rangle$.

As thermal averaging frequently appears in spin relaxation analysis, we define $\langle A\rangle$ as the thermal average of electronic quantity A,

$$\langle A\rangle = \frac{\sum_{kn}(-[f^{eq}]'_{kn})A_{kn}}{\sum_{kn}(-[f^{eq}]'_{kn})} \tag{82}$$

where $[f^{eq}]'$ is the derivative of the Fermi−Dirac distribution function.

According to refs 9. 83, and 84, $\overline{|\tilde{g}^{\uparrow\downarrow}|^2}/\overline{|\tilde{g}^{\uparrow\uparrow}|^2} \sim \langle b^2\rangle$, so that

$$\tau_s^{-1}/\tau_p^{-1} \sim \langle b^2\rangle \tag{83}$$

The above is a rough relation and cannot be used to predict τ_s (the error may be several or even ten times). Practically, we use the following approximate relation

$$\tau_s^{-1}/\tau_p^{-1} = 4\langle b^2\rangle \tag{84}$$

This is called the EY relation in this work.

III.B.3. Spin-–Fip Angle $\theta^{\uparrow\downarrow}$. In our previous paper,[21] we proposed a new electronic quantity important to intervalley spin−flip scattering—the spin−flip angle $\theta^{\uparrow\downarrow}$ between two electronic states. For two states (k,n) and (k',n') with opposite spin directions, $\theta^{\uparrow\downarrow}$ is the angle between $-\mathbf{S}_{kn}^{exp}$ and $\mathbf{S}_{k'n'}^{exp}$. The motivation of examining $\theta^{\uparrow\downarrow}$ is that, according to ref 85, due to time-reversal symmetry, the spin−flip matrix element of the same band between $\mathbf{k}$ and $-\mathbf{k}$ is exactly zero, so that $g^{\uparrow\downarrow}$ is zero at its lowest order for intervalley transitions between two opposite valleys (e.g., $\mathbf{K}$ and $-\mathbf{K}$). In the first-order perturbation level, $|g^{\uparrow\downarrow}|$ between two states is determined by $\theta^{\uparrow\downarrow}$ between these two states and proportional to $|\sin(\theta^{\uparrow\downarrow}/2)|$.

Suppose (i) the inversion symmetry broken induces $\mathbf{B}_k^{in}$ (eq 67) for a Kramers degenerate pair; (ii) there are two valleys centered at wavevectors $\mathbf{Q}$ and $-\mathbf{Q}$; and (iii) k-points $\mathbf{k}_1$ and $\mathbf{k}_2$ are near $\mathbf{Q}$ and $-\mathbf{Q}$, respectively. Due to time-reversal symmetry, the directions of $\mathbf{B}_{k_1}^{in}$ and $\mathbf{B}_{k_2}^{in}$ are almost opposite.

We can prove that for a general operator $\hat{A}$,

$$|A_{k_1k_2}^{\uparrow\downarrow}|^2 \approx \sin^2(\theta_{k_1k_2}^{\uparrow\downarrow}/2)|A_{k_1k_2}^{\downarrow\downarrow}|^2 \tag{85}$$

where $A_{k_1k_2}^{\uparrow\downarrow}$ and $A_{k_1k_2}^{\downarrow\downarrow}$ are the spin−flip and spin-conserving matrix elements between $\mathbf{k}_1$ and $\mathbf{k}_2$, respectively. We present the detailed derivation in supporting information Section SIII of ref 21.

From eq 85, obviously we have

$$|g_{k_1k_2}^{\uparrow\downarrow}|^2 \approx \sin^2(\theta_{k_1k_2}^{\uparrow\downarrow}/2)|g_{k_1k_2}^{\downarrow\downarrow}|^2 \tag{86}$$

Finally, similar to eq 71, we propose an effective modulus square of $\sin(\theta_{k_1k_2}^{\uparrow\downarrow}/2)$,

$$\overline{\sin^2(\theta^{\uparrow\downarrow}/2)} = \frac{\sum_{kq} w_{k,k-q}\sin^2(\theta_{k,k-q}^{\uparrow\downarrow}/2)}{\sum_{kq} w_{k,k-q}} \tag{87}$$

We found spin relaxation time (obtained from our FPDM method) linearly proportional to this quantity $(\overline{\sin^2(\theta^{\uparrow\downarrow}/2)})$ when intervalley spin relaxation process dominates, as an example of substrate effects on spin relaxation of strong SOC Dirac materials in ref 21. Such angle relates to the spin expectation value direction between initial ↑ (↓) and final ↓ (↑) states.

III.C. Dyakonov−Perel (DP) and Free Induction Decay (FID) Mechanisms. *III.C.1. Model Relations.* For nonmagnetic materials, with nonzero k-dependent internal magnetic field $\mathbf{B}_k^{in}$ induced by inversion symmetry broken and spin−orbit coupling, the spins at $\mathbf{k}$ precess about $\mathbf{B}_k^{in}$. The Larmor precession frequency vector can be defined as

$$\mathbf{\Omega}_k = \Delta_k \hat{\mathbf{S}}_k^{exp} \tag{88}$$

where $\hat{\mathbf{S}}_k^{exp}$ is the normalized $\mathbf{S}_k^{exp}$.

We define $\mathbf{\Omega}_{\perp\hat{\mathbf{r}}}$ as the component of $\mathbf{\Omega}$ perpendicular to direction $\hat{\mathbf{r}}$. Suppose the fluctuation amplitude among different k-points of $\mathbf{\Omega}_{\perp\hat{\mathbf{r}}}$ is $\Delta\mathbf{\Omega}_{\perp\hat{\mathbf{r}}}$ and numerically we define it as (using eq 82)

$$\Delta\mathbf{\Omega}_{\perp\hat{\mathbf{r}}} = \sqrt{\langle|\mathbf{\Omega}_{\perp\hat{\mathbf{r}}} - \langle\mathbf{\Omega}_{\perp\hat{\mathbf{r}}}\rangle|^2\rangle} \tag{89}$$

According to refs 7 and8, a nonzero $\Delta\mathbf{\Omega}$ leads to finite spin lifetime $\tau_s^{\Delta\Omega}$ along $\hat{\mathbf{r}}$ and the spin relaxation mechanism depends on the magnitude of $\tau_p\Delta\mathbf{\Omega}$[7,8] (the subindex "$\perp\hat{\mathbf{r}}$" is dropped for simplicity):

(i) DP mechanism if $\tau_p\Delta\mathbf{\Omega} \ll 1$ (strong scattering limit). We have the DP relation

$$(\tau_s^{\Delta\Omega})^{-1} \sim (\tau_s^{DP})^{-1} \sim \tau_p(\Delta\mathbf{\Omega})^2 \tag{90}$$

(ii) FID mechanism if $\tau_p\Delta\Omega \gtrsim 1$ (weak scattering limit). We have

$$(\tau_s^{\Delta\Omega})^{-1} \sim (\tau_s^{FID})^{-1} \sim \Delta\mathbf{\Omega} \tag{91}$$

(iii) Between (i) and (ii) regimes, there is not a good approximate relation for $(\tau_s^{\Delta\Omega})^{-1}$, but we may expect that[8]

https://doi.org/10.1021/acs.jctc.3c00598
J. Chem. Theory Comput. 2024, 20, 492−512

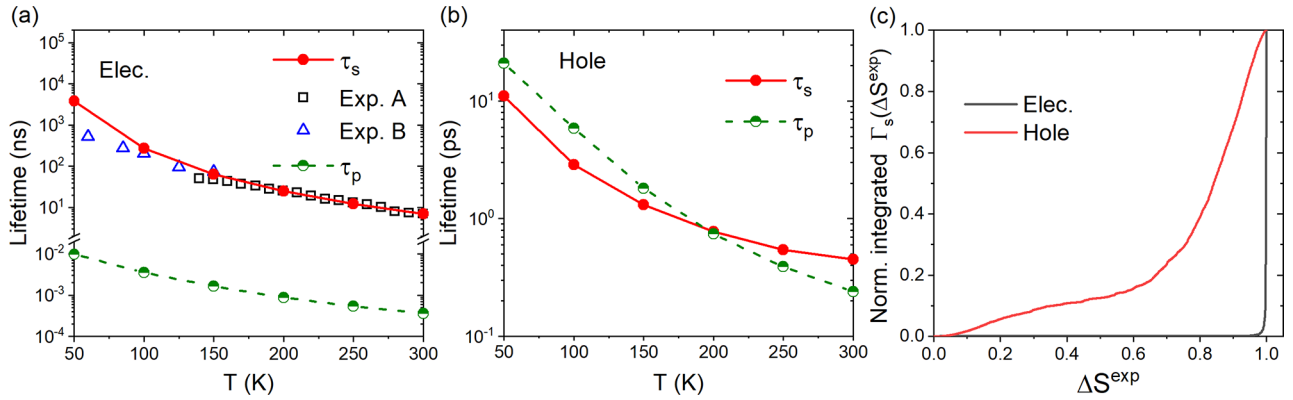

Figure 2. Spin relaxation in silicon (Si). Spin (τ_s) and carrier (τ_p) lifetimes of (a) electrons and (b) holes of Si. "Exp. A" and "Exp. B" are from refs 88 and89. (c) Cumulative contributions to spin relaxation by change of spin expectation value $\Delta\mathbf{S}^{exp}$ per scattering event defined based on eqs 75−77. All spin flip events of Si electrons happen with $\Delta\mathbf{S}^{exp} \approx 1$, whereas spin flip events of Si holes can happen with $\Delta\mathbf{S}^{exp}$ ranging from 0.1 to 1.0. Reprinted with permission from ref 17. Copyright 2020 The Authors under Creative Commons Attribution 4.0 International license, published by Springer Nature.

$$(\tau_s^{DP})^{-1} < (\tau_s^{\Delta\Omega})^{-1} < (\tau_s^{FID})^{-1} \tag{92}$$

III.C.2. Landé g-Factor of Free Carriers. Besides intrinsic spin−orbit coupling, one channel to induce nonzero $\Delta\mathbf{\Omega}$ is through g factor fluctuations under magnetic field. In Section II.A.2, we have described how $\mathbf{B}^{ext}$ is considered in the FPDM approach; therefore, with $H_z(\mathbf{B}^{ext})$, the magnetic-field effects on spin dynamics are straightforwardly included in FPDM simulations.

For the description of the magnetic-field effects, the Landé g-factor has been widely used.[18] For a single band and a pair of bands, the g-factor is well-defined and relates to the $\mathbf{B}^{ext}$-induced change of energy, energy splitting, and/or Larmor precession frequency. In this work, we limit our discussions to two Kramers degenerate bands under a transverse $\mathbf{B}^{ext}$ (perpendicular to the direction of the excess/excited spin $\mathbf{S} \equiv (S_x,S_y,S_z)$). In general, in the two-band case, the g-factor is a tensor and may be defined by the relation $\mathbf{\Omega}_k(\mathbf{B}^{ext}) = \mu_B \mathbf{B}^{ext} g_k^S$. Here, for simplicity, we assume $\mathbf{\Omega}_k(\mathbf{B}^{ext}) \| \mathbf{B}^{ext}$, which is valid in many materials including $CsPbBr_3$. With this assumption and from eq 88,

$$g_k^S = \frac{\mathbf{\Omega}_k(\mathbf{B}^{ext})\cdot\hat{\mathbf{B}}^{ext}}{\mu_B B^{ext}} \tag{93}$$

$\mathbf{\Omega}_k(\mathbf{B}^{ext})$ is computed using eq 88.

However, in many previous theoretical studies,[86,87] g-factors were defined based on pseudospins related to the total magnetic momenta J^{at}, which are determined from the atomic-orbital models. The pseudospins can have opposite directions to the actual spins (S). Most previous experimental studies adopted the same convention for the signs of carrier g-factors. Therefore, to compare with g-factors obtained in those previous studies, we introduce a correction factor $C^{S\to J}$ and define a new g-factor:

$$\tilde{g}_k(\hat{\mathbf{B}}^{ext}) = C^{S\to J} g_k^S \tag{94}$$

$C^{S\to J} = m_S^{at}/m_J^{at}$ with m_J^{at} and m_S^{at} the total and spin magnetic momenta, respectively, obtained from the atomic-orbital model.[87] $C^{S\to J}$ is independent from k-point and is ∓ 1 for electrons and holes, respectively, for $CsPbBr_3$.[18]

As $\tilde{g}_k$ is different at different $\mathbf{k}$, we can define its fluctuation amplitude as

$$\Delta\tilde{g} = \langle(\tilde{g} - \langle\tilde{g}\rangle)^2\rangle \tag{95}$$

From the above equation, we have the fluctuation amplitude of $\Omega_k(\mathbf{B}^{ext})$

$$\Delta\Omega(\mathbf{B}^{ext}) = \mu_B B^{ext} \Delta\tilde{g} \tag{96}$$

A nonzero $\Delta\Omega(\mathbf{B}^{ext})$ leads to spin dephasing under external magnetic field $\mathbf{B}^{ext}$, and the mechanism may be DP or FID depending on the magnitude of $\tau_p\Delta\mathbf{\Omega}$ as discussed above.

III.D. Determination of Spin Relaxation Mechanism. In general, the applicability of our FPDM approach does not depend on a specific spin relaxation mechanism. To determine the dominant relaxation or dephasing mechanism, we have the following two approaches by utilizing our FPDM calculations.

III.D.1. Method 1: Comparing FPDM Calculations with FGR or Model Relations. The first approach is to compare FPDM results directly with simple models designed for various mechanisms as introduced in previous two sections. If FPDM agrees with one of the model relations, it is a good indicator of dominant mechanism.

III.D.1.1. EY Mechanism. Since spin precession is suppressed when the EY mechanism dominates, the DM master equation in semiclassical limit from eq 57 and the FGR formula with spin−flip scattering eq 68 should describe well spin relaxation (suppose the spin matrix is diagonalized in degenerate subspaces along the direction of the excess spin). Therefore, if the values and trends of τ_s by eqs 57 and 68 are similar to those obtained from FPDM calculations, the dominating mechanism is likely the EY.

III.D.1.2. DP or FID Mechanism. With nonzero $\Delta\mathbf{\Omega}$, whether spin relaxation is dominated by DP or FID mechanism may be determined by comparing the values and trends of τ_s by eq 90 or 91 with the FPDM results. We have shown the success of such analysis in our previous work on spin relaxation and transport in germanene and silicene under electric field[19] as well as $CsPbBr_3$ under magnetic field.[18]

III.D.2. Method 2: Tuning the Scattering Strength or Precession Frequency in FPDM Calculations. Conventionally, spin relaxation mechanism is determined from the relation between τ_s and τ_p—the EY mechanism leads to $\tau_s \propto \tau_p$ while the DP mechanism leads to $\tau_s \propto \tau_p^{-1}$. Another way to look at this is through tuning the strength of scatterings (e.g., physically, increasing impurity concentration increases scatter-

https://doi.org/10.1021/acs.jctc.3c00598
J. Chem. Theory Comput. 2024, 20, 492−512

ing). If τ_s decreases with increasing scattering, it is likely EY; otherwise, it is likely the DP mechanism, because τ_p always decreases with increasing scatterings.

Practically in our FPDM calculations, this approach can be implemented by introducing a scaling factor F^{sc} to tune the scattering strength, i.e., multiplying F^{sc} to the scattering term $\left.\frac{d\rho}{dt}\right|_{scatt}$ of the DM master equation (eq 5) but keep the coherent term (the first term of eq 5) unchanged. This is equivalent to multiplying F^{sc} to all elements of the generalized scattering-rate matrix P (eqs 18, 24, and 29).

To avoid confusion, we name carrier and spin lifetimes after introducing F^{sc} as τ_s' and τ_p', respectively. According to eq 59, we always have $\tau_p'/\tau_p = (F^{sc})^{-1}$. On the other hand, τ_s' depends on the spin relaxation mechanism. For the EY mechanism, $\tau_s'/\tau_p' = \tau_s/\tau_p = C^{EY}$, where C^{EY} is a constant unrelated to F^{sc}. Therefore, it can be proven that $\tau_s'/\tau_s = (F^{sc})^{-1} = \tau_p'/\tau_p$. Similarly, for the DP mechanism, we can prove that $\tau_s'/\tau_s = F^{sc} = (\tau_p'/\tau_p)^{-1}$. For the FID mechanism, as τ_s' is irrelevant to τ_p', we have $\tau_s'/\tau_s \equiv 1$. Therefore, the relation between τ_s'/τ_s and τ_p'/τ_p by tuning F^{sc} is useful to understand spin relaxation mechanism.

Moreover, the relation between τ_s and $\Delta\Omega$ is also useful to understand spin relaxation mechanism. $\Delta\Omega$ can be tuned easily by tuning the energy splitting.

IV. APPLICATIONS

IV.A. Nonmagnetic Materials with Inversion Symmetry. Spin relaxation in nonmagnetic materials with inversion symmetry is traditionally described by the EY mechanism. Figure 2a shows that our theoretical electron τ_s of Si are in excellent agreement with experiments.[88,89] Note that in previous first-principles simulations,[9] spin−flip e−ph matrix elements are approximated as the product of spin−flip overlap integral and spin-conserving e−ph matrix element, assuming that the scattering potential varies slowly on the scale of a unit cell, while in our FPDM approach all e−ph matrix elements are directly evaluated using the relativistic electronic wave functions and the scattering potentials with self-consistent SOC. In contrast, holes in Si exhibit strong spin mixing with spin-3/2 character and $|\Delta S_i^{exp}|$ can take various values away from $\pm\hbar/2$ (e.g., $\pm\hbar/6$ at Γ). Figure 2b shows our predicted hole spin lifetimes $\tau_{s,h}$ are much shorter than the electron ones by several orders of magnitude as a result of the strong mixing and is quite close to carrier lifetime τ_p. Moreover, Figure 2c shows that the change of spin expectation values (ΔS^{exp}) per scattering event (evaluated based on eqs 75−77) has a broad distribution for holes of Si, indicating that hole spin relaxation cannot be described by simple spin−flip transitions between a spin-up and spin-down electronic state, while conduction electrons of Si predominantly exhibit spin−flip transitions with $\Delta S^{exp} = 1$.

IV.B. Materials with High-Spin Polarization. In ferromagnets and antiferromagnets, spins are highly polarized, so that spin relaxation is likely mainly driven by spin−flip processes. In ref 17, we simulated τ_s of bcc iron, where we found good agreement with experiments, with a dominant EY mechanism if we do not consider the effect of spin/magnetization fluctuation. In general, spin fluctuation is important to spin dynamics in magnets[12,90] and its effect was simulated by several methods including TDDFT,[12−14] semi-classical Boltzmann equation with rates from FGR,[90] and many-body perturbation theory.[91,92]

In nonmagnetic materials, when inversion symmetry is broken and SOC strength is moderate or large, it has been found that some of them such as transition metal dichalcogenides also have highly polarized carrier spins and exhibit EY spin relaxation.

IV.B.1. Transition Metal Dichalcogenides (TMDs). Monolayer TMDs exhibit exciting features including spin-polarized bands, valley-dependent optical selection rules, and spin−valley locking. In refs 93 and 94, it has been shown that by doping the samples of monolayer TMDs, ultraslow decays of Kerr rotations, which correspond to ultralong spin/valley lifetimes τ_s of resident carriers especially resident holes, can be observed at low temperatures. Those features establish TMDs' advantages for spin−valleytronics and (quantum) information processing. Although τ_s of resident carriers of monolayer TMDs, critical to their spin−valleytronic applications, were extensively examined, the underlying relaxation mechanisms including the effects of realistic impurities have not been addressed through ab initio simulations.

In ref 16, we clarified the above problem by conducting ab initio real-time dynamics simulations with relevant scattering mechanisms. We focused on WSe_2 due to its larger valence band SOC splitting compared with other TMDs and focused on dynamics of resident holes as τ_s of holes seem longer than electrons.

Hole spin/valley relaxation in monolayer WSe_2 is completely determined by intervalley spin−flip scattering between K and K' valleys because of spin−valley locking. Previously, we reported τ_s of resident holes of monolayer TMDs at $T \geq 50$ K with e−ph scattering.[17] At very low temperatures, e.g., 10 K, intervalley e−ph scattering is however not activated as the corresponding phonon occupation is negligible, so that other scattering channels need to be considered. Note that e−e scattering should not play an important role in spin relaxation of holes of TMDs. This is because only the highest valence band is involved in dynamics of TMD holes, so that an e−e scattering process within this band does not change the total spin according to the energy- and momentum-conservation conditions.[16] Therefore, we consider only e−ph and e−i scatterings.

Here we pick four representative types of impurities with different symmetries and chemical bonds (see Figure 3a)—Se vacancy (Se vac.), two neighboring Se vacancies (2N−Se vac.), W vacancy (W vac.), and two Se vacancies with the same in-plane position (2S−Se vac.). n_i of Se vac. is chosen to be 7×10^{11} cm^{-2} within the experimental range,[98−100] which is taken relatively low for better comparison with experimental τ_s (Exp. A in Figure 3b). Since n_i of larger impurities are found lower than smaller impurities,[100] n_i of 2N−Se vac. is chosen to be a rather low value—8×10^9 cm^{-2} (also for better comparison with experimental τ_s). n_i of W vac. and 2S−Se vac. are chosen arbitrarily as their effects on spin relaxation are found to be rather weak and are 7×10^{11} and 3.5×10^{11}cm^{-2}, respectively.

From Figure 3, we first find that assuming n_i are not so high, at $T > 20$ K, spin relaxation is almost driven by e−ph scattering and impurities are only important at $T \leq 20$ K. For the effects on spin relaxation of different impurities, we have 2N−Se vac. ≫ Se vac. ≫ W vac. ∼ 2S−Se vac.. Moreover, the temperature dependence of τ_s with 2N−Se vac. is much weaker and in better agreement with experiments than that with Se vac. Therefore, the observed weak temperature dependence in

https://doi.org/10.1021/acs.jctc.3c00598
J. Chem. Theory Comput. 2024, 20, 492−512

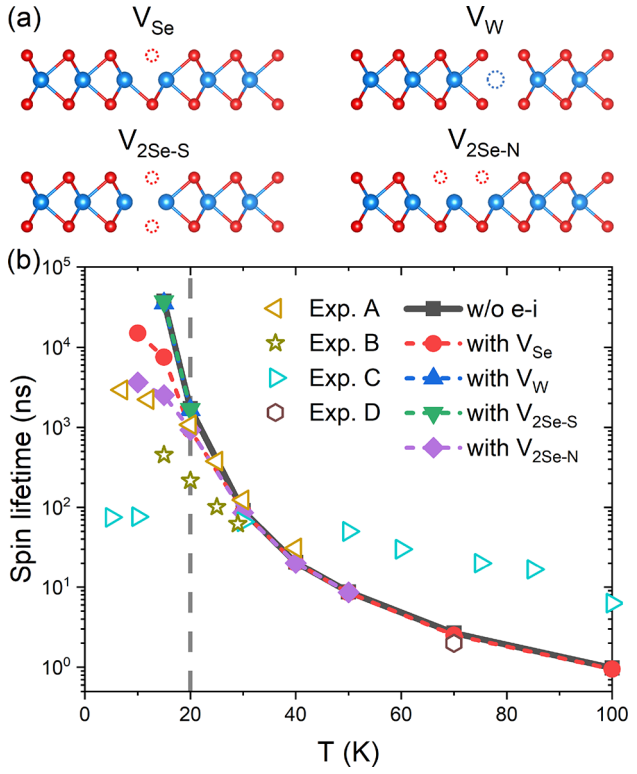

Figure 3. (a) Schematics of four types of impurities in WSe_2. (b) Hole τ_s of monolayer WSe_2 with a low hole density 10^{11} cm^{-2} considering impurities compared with experimental data.[94−97] Adapted with permission from ref 16. Copyright 2021 American Physical Society.

some experiments possibly indicates the existence of larger impurities with lower symmetries. Our results suggest that the local symmetry and chemical bonds surrounding the impurities have a large impact on spin relaxation. To understand why the effects of different impurities on spin relaxation significantly differ, further theoretical investigations on how impurities affect impurity potentials and their SOC corrections are required.

IV.B.2. Germanene under an Electric Field or on a Substrate. In ref 19, through FPDM simulations, we predicted that monolayer germanene (ML-Ge) has giant spin lifetime anisotropy, spin−valley-locking (SVL) effect under nonzero perpendicular electric field E_z and long τ_s (∼100 ns at 50 K), which makes it advantageous for spin−valleytronic applications. In spintronic devices based on 2D materials, the material layers are usually supported by a substrate. Therefore, it is crucial to understand substrate effects on spin relaxation. We thus examined τ_s of ML-Ge on different substrates in ref 21.

Figure 4 shows band structures and spin textures of freestanding and supported ML-Ge, essential for understanding spin relaxation mechanisms discussed below. At E_z = 0, ML-Ge has time-reversal and inversion symmetries, so that its bands are Kramers degenerate.[7] A finite E_z or a substrate breaks the inversion symmetry and induces a strong out-of-plane $\mathbf{B}^{in}$ (and also $\mathbf{S}^{exp}$, eq 67), which splits the Kramers pairs into spin-up and spin-down bands.[19] We find that band structures of ML-Ge-SiH (Figure 4c) and ML-Ge-GeH (not shown) are quite similar to freestanding ML-Ge under E_z = −7 V/nm (ML-Ge@−7 V/nm, Figure 4b). On the other hand, the band structures of ML-Ge-InSe (Figure 4d) and ML-Ge-GaTe (not shown) have more differences from the freestanding one under E_z, with larger band gaps, smaller band curvatures at Dirac cones, and larger electron−hole asymmetry of band splittings. This implies that the impact of the InSe/GaTe substrates cannot be approximated by applying an E_z to the free-standing ML-Ge, unlike SiH/GeH substrates. We further examine $\mathbf{S}^{exp}$ of substrate-supported ML-Ge. Importantly, from Figure 4e,f, although $\mathbf{S}^{exp}$ of ML-Ge on substrates are highly polarized along the z (out-of-plane) direction, the in-plane components of $\mathbf{S}^{exp}$ of ML-Ge-InSe (and ML-Ge-GaTe) are much more pronounced than ML-Ge-SiH (and ML-Ge-GeH). Such differences are crucial to the out-of-plane spin relaxation as discussed later.

We compare out-of-plane τ_s due to e−ph scattering between the freestanding ML-Ge (with/without an electric field) and supported ML-Ge on different substrates in Figure 5. We find that τ_s of ML-Ge under E_z = 0 and −7 V/nm are at the same order of magnitude for a wide range of temperatures. On the other hand, τ_s of supported ML-Ge are very sensitive to the specific substrates. While τ_s of ML-Ge-GeH and ML-Ge-SiH have the same order of magnitude as the freestanding ML-Ge, in particular very close between ML-Ge-GeH and ML-Ge@−7 V/nm, τ_s of ML-Ge-GaTe and ML-Ge-InSe are shorter by at least 1−2 orders of magnitude in the whole temperature range.

Since spins of ML-Ge at $E_z \neq 0$ and on a substrate are highly polarized, spin relaxation in ML-Ge systems is dominated by the EY mechanism. According to eqs 70 and 83, τ_s^{-1} is roughly proportional to density of states (DOS) and spin-mixing parameter $\langle b_z^2 \rangle$. Indeed, in ref 21, we find that, at 300 K, the differences of τ_s of ML-Ge on different substrates are well-explained by the differences of the products of DOS and $\langle b_z^2 \rangle$. However, at $T \leq 50$ K, the differences of the products of DOS and $\langle b_z^2 \rangle$ for different substrates are only about 3−7 times, while the differences of τ_s for different substrates can be as large as 2 orders of magnitude. Therefore, the substrate effects on τ_s cannot be fully explained by the changes of DOS and $\langle b_z^2 \rangle$, in particular at relatively low T.

Since $\tau_s^{-1} \propto \overline{|\tilde{g}^{\uparrow\downarrow}|^2}\, D^S$ (eq 70), to understand substrate effects on τ_s at low T, we first compare τ_s^{-1} and $\overline{|\tilde{g}^{\uparrow\downarrow}|^2}\, D^S$ of different ML-Ge systems. In ref 21, we found that the variation of τ_s^{-1} with the substrate type is well-captured by the variation of $\overline{|\tilde{g}^{\uparrow\downarrow}|^2}\, D^S$ at 20 K. As the variation of D^S is rather weak (at most three times) compared with the large variation of τ_s^{-1} (several orders of magnitude), the substrate-induced change of τ_s should be mostly due to the substrate-induced change of spin−flip matrix elements.

To have deeper intuitive understanding, we then propose a new electronic quantity important to intervalley spin−flip scattering—the spin−flip angle $\theta^{\uparrow\downarrow}$. For two states (k_1,n_1) and (k_2,n_2) with opposite spin directions, $\theta^{\uparrow\downarrow}$ is the angle between $-\mathbf{S}^{exp}_{k_1n_1}$ and $\mathbf{S}^{exp}_{k_2n_2}$ or equivalently the angle between $-\mathbf{B}^{in}_{k_1}$ and $\mathbf{B}^{in}_{k_2}$. The details of $\theta^{\uparrow\downarrow}$ including its relation to the spin−flip matrix elements are given in Section III.B.3.

At low T, due to large SOC splittings of conduction and valence bands of supported ML-Ge, intravalley spin−flip e−ph scattering processes are forbidden, because the corresponding phonons have too high energies and are not occupied. So spin relaxation in supported ML-Ge is dominated by intervalley spin−flip e−ph scattering. Therefore, $\theta^{\uparrow\downarrow}$ is helpful for understanding spin relaxation in supported ML-Ge.

https://doi.org/10.1021/acs.jctc.3c00598
J. Chem. Theory Comput. 2024, 20, 492−512

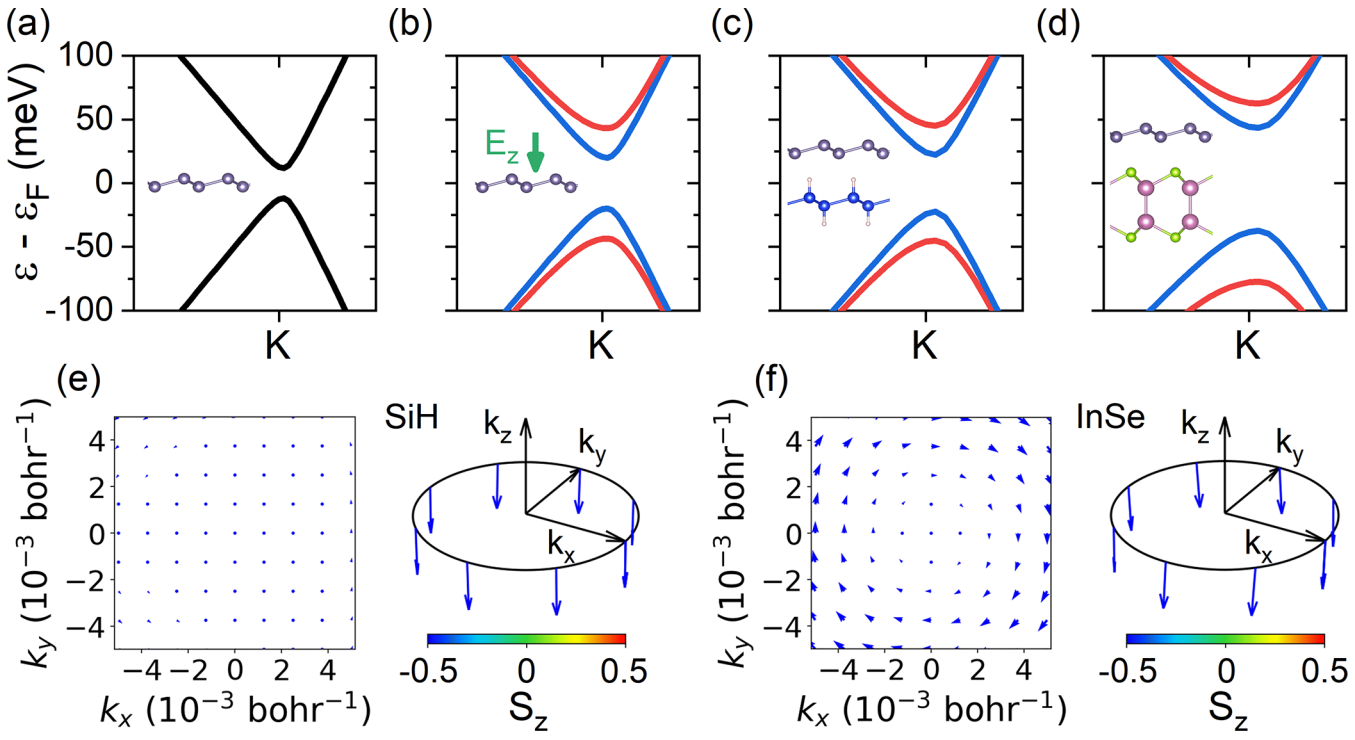

Figure 4. Band structures and spin textures around the Dirac cones of freestanding and supported monolayer germanene (ML-Ge) systems. (a–d) Band structures of ML-Ge under E_z = 0 and under −7 V/nm and ML-Ge on silicane (SiH) and on InSe substrates, respectively. The red and blue bands correspond to spin-up and spin-down states. The gray, white, blue, pink, and green balls correspond to Ge, H, Si, In, and Se atoms, respectively. (e, f) Spin textures in the k_x−k_y plane and 3D plots of the spin vectors $\mathbf{S}_{k_1}^{\text{exp}}$ on the circle $|\vec{k}|$=0.005 bohr^{-1} of the band at the band edge around K of ML-Ge on SiH and InSe substrates, respectively. The color scales S_z^{exp}, and the arrow length scales the vector length of in-plane spin expectation value. Adapted with permission from ref 19. Copyright 2021 American Chemical Society.

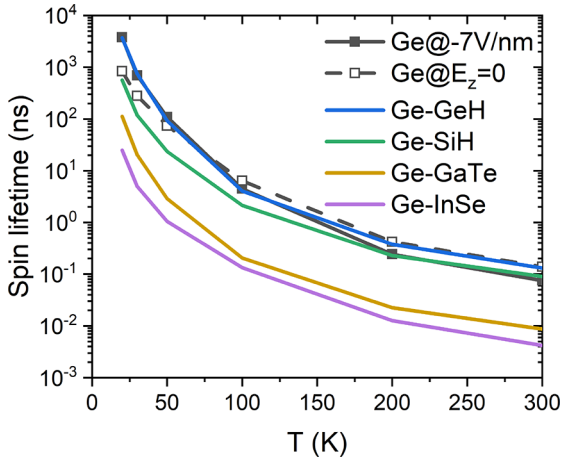

Figure 5. Out-of-plane τ_s of freestanding ML-Ge under E_z = 0, −7 V/nm and supported ML-Ge on several substrates as a function of T without impurities. Adapted with permission from ref 21. Copyright 2023 The Authors under Creative Commons Attribution 4.0 Internation license, published by Springer Nature.

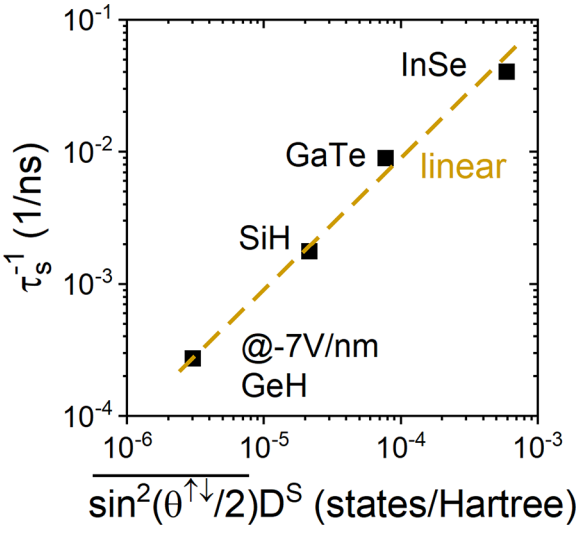

Figure 6. Relation between τ_s^{-1} and $\overline{\sin^2(\theta^{\uparrow\downarrow}/2)}$ multiplied by the scattering density of states D^S at 20 K. D^S is defined in eq 72. $\theta^{\uparrow\downarrow}$ is the spin−flip angle between two electronic states. For two states (k,n) and (k',n') with opposite spin directions, $\theta^{\uparrow\downarrow}$ is the angle between $-\mathbf{S}_{kn}^{\text{exp}}$ and $\mathbf{S}_{k'n'}^{\text{exp}}$. $\overline{\sin^2(\theta^{\uparrow\downarrow}/2)}$ is defined in eq 87. The variation of D^S among different substrates is at most three times, much weaker than the variations of τ_s^{-1} and other quantities shown here. Adapted with permission from ref 21. Copyright 2023 The Authors under Creative Commons Attribution 4.0 International license, published by Springer Nature.

As shown in Figure 6c, τ_s^{-1} of ML-Ge on different substrates at 20 K is almost linearly proportional to $\overline{\sin^2(\theta^{\uparrow\downarrow}/2)}D^S$, where $\overline{\sin^2(\theta^{\uparrow\downarrow}/2)}$ is the statistically averaged modulus square of $\sin(\theta^{\uparrow\downarrow}/2)$. This indicates that the relation $\overline{|\tilde{g}^{\uparrow\downarrow}|^2} \propto \overline{\sin^2(\theta^{\uparrow\downarrow}/2)}$ is nearly perfectly satisfied at low T, where intervalley processes dominate spin relaxation. We additionally examined the relation between τ_s^{-1} and

https://doi.org/10.1021/acs.jctc.3c00598
J. Chem. Theory Comput. 2024, 20, 492−512

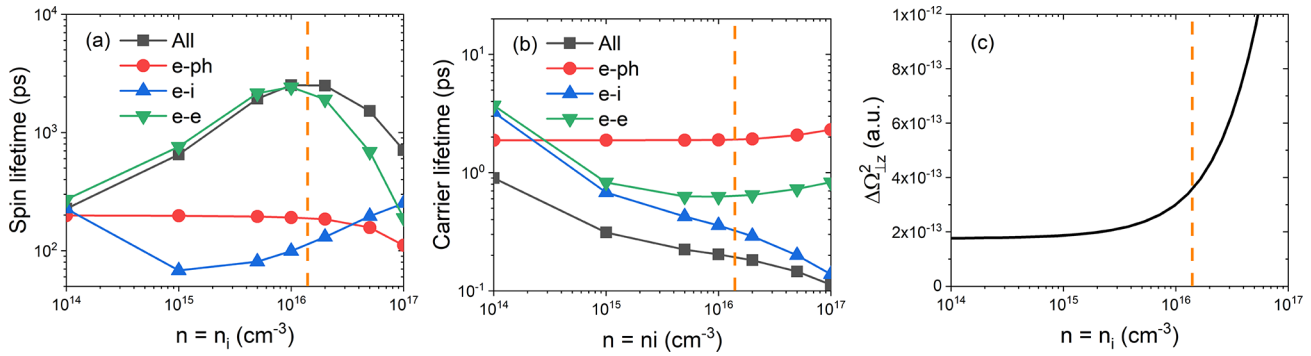

Figure 7. (a) τ_s and (b) τ_p of *n*-GaAs with different doping concentrations n_i at 30 K with different scattering mechanisms. "All" represents all of the e−ph, e−i, and e−e scattering mechanisms being considered. (c) $\Delta\Omega_{\perp z}{}^2$ as a function of carrier density *n*, where $\Delta\boldsymbol{\Omega}_{\perp z}$ is the fluctuation amplitude of Larmor frequency defined in eq 89. Adapted with permission from ref 16. Copyright 2021 American Physical Society.

$\overline{\sin^2(\theta^{\uparrow\downarrow}/2)}D^S$ at 300 K and found that the trend of τ_s^{-1} is still approximately captured by the trend of $\overline{\sin^2(\theta^{\uparrow\downarrow}/2)}D^S$.

Since $\theta^{\uparrow\downarrow}$ is defined by $\mathbf{S}^{\text{exp}}$ at different states, τ_s is highly correlated with $\mathbf{S}^{\text{exp}}$ and more specifically with the anisotropy of $\mathbf{S}^{\text{exp}}$ (equivalent to the anisotropy of $\mathbf{B}^{\text{in}}$). Qualitatively, the larger anisotropy of $\mathbf{S}^{\text{exp}}$ leads to smaller $\theta^{\uparrow\downarrow}$ (consistent with Figure 4e,f) and longer τ_s along the high-spin-polarization direction. This finding may be applicable to spin relaxation in other materials whenever intervalley spin−flip scattering dominates or spin−valley locking exists, e.g., in TMDs,[93] stanene,[101] 2D hybrid perovskites with persistent spin helix,[6] etc.

IV.C. DP (Dyakonov−Perel) Systems. In many nonmagnetic materials with broken inversion symmetry, spin relaxation is dominated by the DP mechanism.

IV.C.1. GaAs. Spin dynamics in GaAs has broad interest in spintronics,[7,25,102−107] partly due to its long τ_s in n-type GaAs at low temperatures.[25] Despite various experimental[25,51,102,108,109] and theoretical[7,103,104,110−112] (mostly using parametrized model Hamiltonian) studies previously, the dominant spin relaxation mechanism in bulk GaAs at various *T* and doping concentrations n_i remains unclear.

Through FPDM simulations of *n*-GaAs at various *T* and n_i with different scattering mechanisms in ref 16, we pointed out that although at low temperatures and moderate doping concentrations e−i scattering dominates carrier relaxation, e−e scattering is the most dominant process in spin relaxation.

Figure 7 shows τ_s and τ_p with different n_i at 30 K with individual and total scattering pathways, respectively. It is found that the roles of different scattering mechanisms differ considerably between spin and carrier relaxation processes. Specifically, for the carrier relaxation in Figure 7b, except when n_i is very low (e.g., at 10^{14} cm^{-3}), the e−i scattering dominates. On the other hand, for the spin relaxation in Figure 7a, the e−e scattering dominates except at very high concentration (above 10^{17} cm^{-3}).

Figure 7 shows the calculated τ_s has a maximum at $n_i = (1-2) \times 10^{16}$ cm^{-3}, and τ_s decreases fast with n_i going away from its peak position. This is in good agreement with the experimental finding in ref 25, which also reported τ_s at $n_i = 10^{16}$ cm^{-3} is longer than τ_s at other lower and higher n_i at a low temperature (a few kelvin). The n_i dependence of τ_s may be qualitatively interpreted from the DP relation[7] $\tau_{s,z} \sim \tau_p \Delta\Omega_{\perp z}{}^2$ (eq 90), where $\Delta\boldsymbol{\Omega}_{\perp z}$ is the fluctuation amplitude of Larmor frequency defined in eq 89. From Figure 7, we find that with n_i from 10^{14} to 5×10^{15} cm^{-3}, τ_p decreases rapidly (black curve in Figure 7b) and $\Delta\Omega_{\perp z}^2$ remains flat in Figure 7c, which may explain why τ_s increases in Figure 7a based on the DP relation; however, when $n_i > 10^{16}$ cm^{-3}, τ_p decreases with a similar speed but $\Delta\Omega_{\perp z}{}^2$ experiences a sharp increase, which may explain why τ_s decreases in Figure 7b and owns a maximum at 10^{16} cm^{-3}.

IV.C.2. Graphene on hBN. Graphene samples exhibit exciting spintronic properties such as long τ_s and l_s at room temperature.[1,113] In practice, graphene is usually supported by a substrate.[113−117] Actually τ_s of the freestanding graphene sample was found relatively low,[118] ∼150 ps at 300 K (compared with the longest reported value of ∼12 ns), probably due to freestanding graphene samples often having more imperfections. Therefore, it is important to understand spin relaxation in supported graphene.

From Figure 8, we find that the EY model for graphene and the DP model for Gr+$E_\perp$ and Gr−hBN agree qualitatively with FPDM predictions, but with some important quantitative differences discussed next. First, the EY model for graphene is more accurate for electrons than for holes, for both $\tau_{s\parallel}$ and $\tau_{s\perp}$ (Figure 8a,b). The conventional DP model matches FPDM predictions quantitatively for both $\tau_{s\parallel}$ and $\tau_{s\perp}$ of Gr+$E_\perp$, but only for $\tau_{s\perp}$ of Gr−hBN.

The discrepancy of the conventional DP model for $\tau_{s\parallel}$ of Gr−hBN can be rectified by modifying the model. Briefly, the DP model assumes that $\mathbf{B}^{\text{in}}$ effectively changes randomly each time the electron scatters. The in-plane magnetic field $\mathbf{B}_\parallel^{\text{in}}$ rotates over the Fermi circle and covers all in-plane directions, satisfying this condition, in both Gr+$E_\perp$ and Gr−hBN. However, the out-of-plane magnetic field $\mathbf{B}_\perp^{\text{in}}$, which matters only for $\tau_{s\parallel}$ and is present only for Gr−hBN, has the same direction within each valley. Consequently, only intervalley scattering will change the $\mathbf{B}_\perp^{\text{in}}$ for a given electron spin. As proposed in ref 119, this can be captured by changing the DP model from $(\tau_{s,x}^{\text{DP}})^{-1} \sim \tau_p(\Delta\boldsymbol{\Omega}_{\perp x})^2 = \tau_p\langle\Omega_y{}^2 + \Omega_z{}^2\rangle$ as given by eq 90 for in-plane *x* spins, to

$$(\tau_{s,x}^{\text{mDP}})^{-1} \approx \tau_p\langle\Omega_y{}^2\rangle + \tau_p^{\text{Inter}}\langle\Omega_z{}^2\rangle \tag{97}$$

where τ_p^{Inter} is the intervalley scattering time (dotted line in Figure 8d). This modified DP model agrees with FPDM predictions for $\tau_{s\parallel}$ of Gr−hBN (Figure 8a).

The ratio $\tau_{s\perp}/\tau_{s\parallel}$ (Figure 8c) is nearly 1/2 for graphene, consistent with the EY relation eq 83 and the fact that $\langle b_\parallel{}^2\rangle/\langle b_\perp{}^2\rangle$ is also 1/2 (Figure 8e). This ratio remains unchanged for Gr+$E_\perp$, but now because $(\Delta\boldsymbol{\Omega}_{\perp z})^2 = \langle\Omega_x{}^2 + \Omega_y{}^2\rangle = 2\langle\Omega_y{}^2\rangle$,

https://doi.org/10.1021/acs.jctc.3c00598
J. Chem. Theory Comput. 2024, 20, 492−512

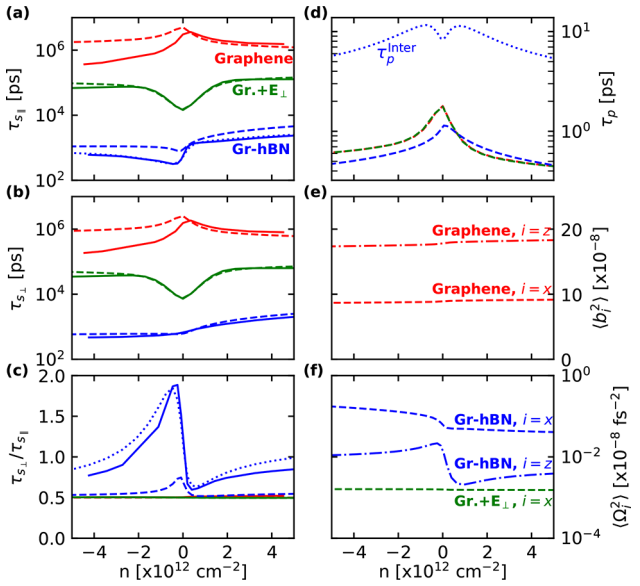

Figure 8. Theoretical spin and carrier relaxation in graphene (red lines), graphene at $E_\perp$ = 0.4 V/nm (Gr+$E_\perp$, green lines), and graphene on hBN (Gr−hBN, blue lines) as a function of n (positive or negative for electron and hole doping, respectively) at room temperature. (a) In-plane spin lifetime $\tau_{s\parallel}$, (b) out-of-plane spin lifetime $\tau_{s\perp}$, and (c) their ratios $\tau_{s\perp}/\tau_{s\parallel}$ calculated using FPDM approach (solid lines) compared with those estimated from EY/DP models with first-principles inputs (dashed for conventional DP and dotted for modified DP with intervalley scattering contribution lines). (d) Total τ_p (three dashed lines) and intervalley only contribution for Gr−hBN (dotted blue line), (e) $\langle b_i^2\rangle$ and (f) $\langle\Omega_i^2\rangle$, all predicted from first-principles for the DP and EY model estimates of τ_s in panels a−c. Adapted with permission from ref 20. Copyright 2022 American Physical Society.

while $(\Delta\boldsymbol{\Omega}_{\perp x})^2 = \langle\Omega_y{}^2\rangle$ since $\Omega_z = 0$ (Figure 8f), leading to $\tau_{s,x}^{DP} = 2\tau_{s,z}^{DP}$ using eq 90. This ratio deviates substantially from 1/2 only for Gr−hBN (Figure 8c) due to the substrate-induced $\Omega_z \neq 0$. The conventional DP model (eq 90) only captures part of this dramatic effect seen in the FPDM calculations, while the modifications in eq 97 account for Ω_z correctly and agree with the FPDM results in Figure 8c.

τ_s decreases with increasing carrier density magnitude in graphene (Figure 8a,b), but this trend reverses for both inversion-symmetry-broken cases, in agreement with some experiments.[113,120] The overall τ_s are reduced by 1−2 orders of magnitude in freestanding graphene by $E_\perp$ of 0.4 V/nm, down from μs to tens of ns. $\langle\Omega_i^2\rangle$ of Gr−hBN in Figure 8f is about 100 times larger than that of Gr+$E_\perp$, further reducing τ_s of Gr−hBN to the ns scale, comparable to experimental measurements.[113,115,116,121]

Finally, τ_s is mostly symmetric between electrons and holes for Gr+$E_\perp$ (Figure 8a,b). However, we find hole τ_s to be typically 2−3 times smaller than electrons for both freestanding graphene and Gr−hBN. On hBN, this asymmetry is captured by the (modified) DP model and stems primarily from the larger spin-splitting and hence $\langle\Omega_i^2\rangle$ in the valence band compared to the conduction band (not shown), consistent with previous calculations.[122] Importantly, this effect depends sensitively on the substrate and, even on hBN, could reverse for a different layer stacking.[122] Consequently, experiments may find electron−hole asymmetries of either sign depending on the substrate and precise structure,[113,115−117,120−122] and we focus here on the comparison between FPDM predictions and the DP model for the specific lowest-energy stacking of Gr-hBN.

In our work, we simulate τ_s of clean Gr−hBN free from impurities. However, it is well-known that both nonmagnetic and magnetic impurities play important roles in spin relaxation in both freestanding and substrate-supported graphene.[10,47,123] With inversion symmetry broken, the inclusion of the e−i scattering may decrease or increase τ_s of Gr−hBN through EY and DP spin relaxation. Therefore, it is interesting and crucial to study how τ_s of Gr−hBN are affected by different types of impurities. The inclusion of nonmagnetic impurities is straightforward in our FPDM approach as described in Section II.A.3, which will be our future work.

IV.D. Spin Dephasing under Magnetic Field. As introduced in Section II.B.1, the dephasing time (or transverse time) of a spin ensemble is called T_2^* and describes the decay of the total excess spin $\mathbf{S} - \mathbf{S}^{eq}$ at an nonzero $\mathbf{B}^{ext}$ perpendicular to $\mathbf{S} - \mathbf{S}^{eq}$. As discussed in Section II.A.2, T_2^* can be simulated straightforwardly through FPDM simulations with Zeeman Hamiltonian considering both spin and orbital angular momenta (eqs 13 and 14). For the purpose of analyzing and understanding spin dephasing, one key parameter is the Landé g-factor $\tilde{g}$ (eq 94). Its value relates to $\mathbf{B}^{ext}$-induced energy splitting (Zeeman effect) $\Delta E(\mathbf{B}^{ext})$ and Larmor precession frequency Ω, satisfying $\Omega \approx \Delta E = \mu_B B^{ext}\tilde{g}$. More importantly, the g-factor fluctuation (near Fermi surface or $\mu_{F,c}$) $\Delta\tilde{g}$ (eq 95) leads to a nonzero $\Delta\Omega$ (eq 96) and then T_2^* due to DP or FID mechanism.

Spintronics in halide perovskites has drawn significant attention in recent years, due to highly tunable spin−orbit fields and intriguing interplay with lattice symmetry. Recently, we have simulated[18] $\tilde{g}$, $\Delta\tilde{g}$, and T_2^* of a typical halide perovskite—$CsPbBr_3$. We find that T_2^* is sensitive to B^{ext} at T < 20 K but not at $T \geq 20$ K. At 4 K, we predict that $(T_2^*)^{-1}$ is linear to B^{ext} at $B^{ext} \geq 0.4$ T and the predicted slope of $(T_2^*)^{-1}$ is in good agreement with experimental data. Moreover, we predict strong n-dependence of $\tilde{g}$, $\Delta\tilde{g}$, and T_2^*. Together with FPDM simulations of spin relaxation time T_1 of $CsPbBr_3$ at various conditions, our work provides fundamental insights on how to control and manipulate spin relaxation/dephasing in halide perovskites, which are vital for their spintronics and quantum information applications.

V. OUTLOOKS

V.A. Method Development. The first-principles density-matrix dynamics (FPDM) approach is an important technique for studying spin and electron dynamics and transport, with outstanding advantages: (i) it can accurately describe various interactions, scattering processes, and spin precession simultaneously; (ii) it can describe processes far from equilibrium; (iii) it can simulate dynamical processes on various time scales from femtoseconds to milliseconds. We have shown its success in simulating ultrafast spin dynamics, spin and charge transport, relaxation, and dephasing. In the future study, the FPDM approach still has a broad open area for new theory development.

V.A.1. Exciton Dynamics. Exciton is a bound electron−hole pair generated by optical excitation. Excitons play an important role in optical properties of semiconductors, in particular in low-dimensional systems. Exciton dynamics has been extensively studied using different methods, in particular non-

https://doi.org/10.1021/acs.jctc.3c00598
J. Chem. Theory Comput. 2024, 20, 492−512

equilibrium Green's function theory (NEGF) within Kadanoff−Baym equations.[52,74,124] We focus on theoretical simulations of exciton spin relaxation based on Lindbladian DM master equation with quantum description of the exciton−phonon scattering. Understanding the exciton spin relaxation is also important for understanding optical measurements of spin dynamics. By replacing electrons to excitons, the existing FPDM approach can be generalized to simulation spin dynamics of excitons. The exciton dynamics can involve many types of processes including exciton−light interaction, exciton−phonon scattering, phonon-mediated exciton recombination and dissociation, exciton−exciton annihilation, etc. Initially, we will focus on exciton−light interaction and exciton−phonon scattering, which are the two most important processes leading to exciton spin relaxation.

The exciton−light interaction is responsible to exciton spin generation by light absorption with a circularly polarized pump pulse and exciton spin relaxation through exciton−phonon scattering and exciton radiative recombination. The light absorption for excitons is similar to that for electrons (see Section II.A.2) except that the momentum matrix elements are now between two excitonic states.[125−127]

The exciton−phonon scattering is responsible to exciton spin relaxation. According to refs 128 and 129, the exciton−phonon scattering matrix elements can be approximately obtained from the exciton wave function at finite momentum and electron−phonon scattering matrix elements. Recently we implemented the exciton−phonon scattering matrix elements and used them to simulate phonon-assisted indirect exciton radiative recombination. In the density-matrix master equation, the term of the exciton−phonon scattering is rather similar to the electron−phonon scattering, except that the excitons are bosons while the electrons are fermions. Therefore, the implementation of the exciton−phonon scattering in the frame of FPDM approach can be straightforward.

V.A.2. Circular Photogalvanic Effect (CPGE). CPGE is the effect that under the circularly polarized light a DC current may be induced in a solid-state material, and widely presents in materials without inversion symmetry, in the absence of p−n junction and applied electric field. In recent years, CPGE has attracted growing interests in the fields of topological physics and spin-optotronics.[130,131] In order to deeply understand CPGE, theoretical methods have been developed based on perturbation theory. However, several critical issues remain: (i) the scattering mechanisms are highly simplified with a single relaxation time approximation; (ii) spontaneous recombination was rarely considered; (iii) available theory requires different formulation for each contribution, i.e., interband or intraband contributions; (iv) many-body effects were not considered. These issues may be resolved based on our FPDM approach.

If a constant laser field is applied to an inversion-symmetry-broken system, the quantum master equation for describing the density matrix of the electronic system reads as

$$\frac{\mathrm{d}\rho}{\mathrm{d}t} = \left.\frac{\mathrm{d}\rho}{\mathrm{d}t}\right|_{\mathrm{laser}} + \left.\frac{\mathrm{d}\rho}{\mathrm{d}t}\right|_{\mathrm{sp-em}} + \left.\frac{d\rho}{\mathrm{d}t}\right|_{\mathrm{e-ph}} \tag{98}$$

where $\left.\frac{\mathrm{d}\rho}{\mathrm{d}t}\right|_{\mathrm{laser}}$ is coherent dynamics due to a laser field (eq 12) and $\left.\frac{\mathrm{d}\rho}{\mathrm{d}t}\right|_{\mathrm{sp-em}}$ and $\left.\frac{\mathrm{d}\rho}{\mathrm{d}t}\right|_{\mathrm{e-ph}}$ are the spontaneous emission (eq 37) and e−ph scattering terms (eqs 16 and 18), respectively.

CPGE is measuring the steady-state current when a nonmagnetic system is under a constant circularly polarized laser field for a long enough time. In the velocity gauge, the current density is computed using[37]

$$\mathbf{J}=\mathrm{Tr}(\rho\mathbf{j}) \tag{99}$$

$$\mathbf{j}_{kmn}(t)=-e\left(\mathbf{v}_{kmn} + \delta_{mn}\frac{e}{m_{\mathrm{e}}}\mathbf{A}(t)\right) \tag{100}$$

where $\mathbf{v}$ is the velocity operator matrix and $\mathbf{v} = \mathbf{p}/m_{\mathrm{e}}$.

V.A.3. More on Scattering Terms. Although, in our FPDM approach, the ab initio treatment of quantum scattering is rather general, the following theoretical development can further improve the applicability of our methods to different systems:

V.A.3.1. Anharmonic Phonons. In current implementation, phonons are harmonic and it is required that the material must be dynamically stable at zero temperature. However, for some soft materials (e.g., hybrid halide perovskites), significant anharmonic effects appear at high-T phase, which requires extracting phonon properties from finite-temperature simulations, e.g., using ab initio molecular dynamics. Such an approach has been implemented[132] for studying phonon, electron−phonon, and carrier transport properties, which can be also applied to study the anharmonic effect on spin relaxation under our FPDM framework.

V.A.3.2. Fröhlich Interaction and LO−TO Splitting in Doped Semiconductor. The intraband dielectric screening is not considered for Fröhlich interaction and LO−TO splitting in current implementation. This may be problematic in doped semiconductor and may lead to significant errors at moderate or high carrier density. Since we have already implemented the intraband RPA dielectric function, its effect can be straightforwardly included in the FPDM approach similar to that in ref 133.

V.A.3.3. Short-Range Contribution to the Electron−Ionized-Impurity Scattering. For the electron-ionized-impurity scattering, we currently only consider the long-range contribution. This is appropriate for certain systems like GaAs but may be problematic when intervalley processes dominate spin relaxation or the short-range spin−flip electron-ionized-impurity scattering is unimportant to spin relaxation. Therefore, it is important to include both long-range and short-range contributions to the electron-ionized-impurity scattering. Similar to ref 61, the long-range and short-range parts are treated separately—the short-range part is treated from first-principles similar to neutral impurity, and the long-range part is simulated using the screened Coulomb potential.

V.B. Spintronics Materials. *V.B.1. Graphene Derivatives.* Graphene is a "star" material in the field of spintronics. It exhibits long spin lifetime and diffusion length, high carrier mobility, and an ideal material platform for rich physics.[134] Spin dynamics and transport in graphene derivatives, including van der Waals graphene heterostructures and metal intercalated graphene, have been widely studied both experimentally and theoretically.[1,2,135,136] While most theoretical simulations of spin relaxation and diffusion were carried out by model Hamiltonian methods, ab initio simulations of τ_s and l_s of graphene were scarce and only considered the EY mechanism and the e−i scattering.[10] Therefore, our FPDM approach serves as an invaluable tool to answer some important questions of spin relaxation in graphene, which have not

https://doi.org/10.1021/acs.jctc.3c00598
J. Chem. Theory Comput. 2024, 20, 492−512

been fully resolved. For instance, (i) how do substrates or the formation of heterostructures affect τ_s, l_s, and their anisotropy of graphene? The anisotropy and its variation with the density and temperature are helpful information for the understanding of spin relaxation mechanisms.[117] (ii) What are the upper limits of τ_s and l_s of graphene heterostructures and how do they vary with external conditions? Such information is critical to the search of promising spintronic materials but is hard to obtain from the measurements. (iii) What are the effects of point defects (at graphene or substrates and of different types) on τ_s and l_s of graphene and its heterostructures? This is helpful for optimizing the materials synthesis and fabrication. (iv) And what are the differences of spin dynamics and transport in multilayer and monolayer graphene, and how does the stacking angle change the results?

V.B.2. Halide Perovskites. In ref 18, we studied spin relaxation and dephasing in halide perovskites with inversion symmetry. We also examined the effects of inversion symmetry broken by introducing model SOC fields into the centrosymmetric $CsPbBr_3$. Although this provides helpful mechanistic insights into the symmetry effects, it does not provide accurate predictions of specific materials. Systematic ab initio simulations of spin properties including τ_s and l_s of other halide perovskites with various symmetries, dimensionalities, and chemical compositions are demanded for halide−perovskite spintronics.

Moreover, with the implementations of exciton dynamics and CPGE based on our FPDM approach mentioned above, the corresponding spin dynamic and transport properties of halide perovskites can be predicted, which is also of great interest in the field of halide−perovskite spintronics.

In ref 18, it was pointed out that although the fluctuation of g-factor (and the resulting T_2^*) is not so sensitive to exchange−correlation potential V_{xc}, the magnitude of the g-factor is rather sensitive to V_{xc}. For example the PBE values of electron and hole g-factors of bulk $CsPbBr_3$ has large discrepancy from experimental data while the EV93PW91 values are much closer to them. This V_{xc} dependence may be mitigated by including the nonlocal electron self-energy effect within the GW approximation.[137] Moreover, our theoretical results also show that although V_{xc} does not change the order of magnitude of T_1, it does change T_1 of several halide perovskites by up to tens of percent at high temperatures, and a few times at low temperatures. Therefore, future theoretical studies are required to better understand the V_{xc} dependence of spin properties of halide perovskites.

V.B.3. Persistent Spin Helix (PSH). In materials with spin texture of persistent spin helix,[6,138,139] e.g., $BiInO_3$, WO_2Cl_2, and 2D hybrid perovskites,

$$\mathbf{B}^{\text{in}} = \alpha^{\text{PSH}} k_i \hat{\mathbf{j}} \tag{101}$$

where α^{PSH} denotes a materials-dependent constant related to SOC strength, direction i is perpendicular to $\hat{\mathbf{j}}$, and k_i is relative to a high-symmetry k-point $\mathbf{k}_{\text{center}}$. Such $\mathbf{B}^{\text{in}}$ suppresses spin relaxation and diffusion through the DP mechanism[6] when parallel to the spin helix. When α is large, e.g., in 2D hybrid perovskites with Pb, the band edges are located at two opposite k-points far away from $\mathbf{k}_{\text{center}}$, so that intervalley spin−flip scattering may be important in spin relaxation and diffusion. When below a critical temperature, spin−valley locking can be realized, as discussed in Sections III.B.3 and IV.B.2. Meanwhile if the averaged spin−flip angle $\theta^{\uparrow\downarrow}$ is tiny, τ_s of PSH materials can be long. Through FPDM simulations, we will predict τ_s and l_s of PSH materials and reveal the key factors determine these properties.

AUTHOR INFORMATION

Corresponding Author

Yuan Ping − *Department of Materials Science and Engineering, University of Wisconsin—Madison, Madison, Wisconsin 53706, United States; Department of Physics, University of California, Santa Cruz, California 95064, United States;* orcid.org/0000-0002-0123-3389; Email: yping3@wisc.edu

Author

Junqing Xu − *Department of Physics, Hefei University of Technology, Hefei 230031 Anhui, China; Department of Chemistry and Biochemistry, University of California, Santa Cruz, California 95064, United States*

Complete contact information is available at: https://pubs.acs.org/10.1021/acs.jctc.3c00598

Notes

The authors declare no competing financial interest.

ACKNOWLEDGMENTS

This work is supported by National Science Foundation under Grant No. DMR-1956015. This research used resources of the Center for Functional Nanomaterials, which is a U.S. Department of Energy (DOE) Office of Science facility; the Scientific Data and Computing Center, a component of the Computational Science Initiative, at Brookhaven National Laboratory under Contract No. DE-SC0012704; the lux supercomputer at UC Santa Cruz, funded by NSF MRI Grant AST 1828315; the National Energy Research Scientific Computing Center (NERSC), a U.S. DOE Office of Science user facility operated under Contract No. DE-AC02-05CH11231; and the Extreme Science and Engineering Discovery Environment (XSEDE), which is supported by National Science Foundation Grant No. ACI-1548562.[140]

REFERENCES

(1) Avsar, A.; Ochoa, H.; Guinea, F.; Özyilmaz, B.; van Wees, B. J.; Vera-Marun, I. J. Colloquium: Spintronics in Graphene and Other Two-Dimensional Materials. *Rev. Mod. Phys.* **2020**, *92*, No. 021003.

(2) Sierra, J. F.; Fabian, J.; Kawakami, R. K.; Roche, S.; Valenzuela, S. O. Van der Waals heterostructures for spintronics and opto-spintronics. *Nat. Nanotechnol.* **2021**, *16*, 856−868.

(3) Garcia, J. H.; Vila, M.; Hsu, C.-H.; Waintal, X.; Pereira, V. M.; Roche, S. Canted persistent spin texture and quantum spin Hall effect in WTe_2. *Phys. Rev. Lett.* **2020**, *125*, No. 256603.

(4) Šmejkal, L.; Mokrousov, Y.; Yan, B.; MacDonald, A. H. Topological antiferromagnetic spintronics. *Nat. Phys.* **2018**, *14*, 242−251.

(5) Kim, Y.-H.; Zhai, Y.; Lu, H.; Pan, X.; Xiao, C.; Gaulding, E. A.; Harvey, S. P.; Berry, J. J.; Vardeny, Z. V.; Luther, J. M.; Beard, M. C. Chiral-induced spin selectivity enables a room-temperature spin light-emitting diode. *Science* **2021**, *371*, 1129−1133.

(6) Zhang, L.; Jiang, J.; Multunas, C.; Ming, C.; Chen, Z.; Hu, Y.; Lu, Z.; Pendse, S.; Jia, R.; Chandra, M.; Sun, Y.-Y.; Lu, T.-M.; Ping, Y.; Sundararaman, R.; Shi, J. Room-temperature electrically switchable spin−valley coupling in a van der Waals ferroelectric halide perovskite with persistent spin helix. *Nat. Photonics* **2022**, *16*, 529−537.

(7) Zutic, I.; Fabian, J.; Das Sarma, S. Spintronics: Fundamentals and Applications. *Rev. Mod. Phys.* **2004**, *76*, 323−410.

(8) Wu, M.; Jiang, J.; Weng, M. Spin dynamics in semiconductors. *Phys. Rep.* **2010**, *493*, 61−236.

(9) Restrepo, O. D.; Windl, W. Full first-principles theory of spin relaxation in group-IV materials. *Phys. Rev. Lett.* **2012**, *109*, No. 166604.
(10) Fedorov, D. V.; Gradhand, M.; Ostanin, S.; Maznichenko, I. V.; Ernst, A.; Fabian, J.; Mertig, I. Impact of Electron-Impurity Scattering on the Spin Relaxation Time in Graphene: A First-Principles Study. *Phys. Rev. Lett.* **2013**, *110*, No. 156602.
(11) Marques, M. A. L., Maitra, N. T., Nogueira, F. M. S., Gross, E. K. U., Rubio, A., Eds. *Fundamentals of Time-Dependent Density Functional Theory*; Lecture Notes in Physics, Vol. *837*; Springer Science & Business Media, 2012. DOI: 10.1007/978-3-642-23518-4.
(12) Chen, Z.; Wang, L. Role of Initial Magnetic Disorder: A Time-Dependent Ab Initio Study of Ultrafast Demagnetization Mechanisms. *Sci. Adv.* **2019**, *5*, No. eaau8000.
(13) Acharya, S. R.; Turkowski, V.; Zhang, G. P.; Rahman, T. S. Ultrafast Electron Correlations and Memory Effects at Work: Femtosecond Demagnetization in Ni. *Phys. Rev. Lett.* **2020**, *125*, No. 017202.
(14) Krieger, K.; Dewhurst, J. K.; Elliott, P.; Sharma, S.; Gross, E. K. U. Laser-Induced Demagnetization at Ultrashort Time Scales: Predictions of TDDFT. *J. Chem. Theory Comput.* **2015**, *11*, 4870−4874.
(15) Park, J.; Zhou, J.-J.; Luo, Y.; Bernardi, M. Predicting Phonon-Induced Spin Decoherence from First Principles: Colossal Spin Renormalization in Condensed Matter. *Phys. Rev. Lett.* **2022**, *129*, No. 197201.
(16) Xu, J.; Habib, A.; Sundararaman, R.; Ping, Y. Ab initio ultrafast spin dynamics in solids. *Phys. Rev. B* **2021**, *104*, No. 184418.
(17) Xu, J.; Habib, A.; Kumar, S.; Wu, F.; Sundararaman, R.; Ping, Y. Spin-Phonon Relaxation from a Universal Ab Initio Density-Matrix Approach. *Nat. Commun.* **2020**, *11*, 2780.
(18) Xu, J.; Li, K.; Huynh, U. N.; Huang, J.; Sundararaman, R.; Vardeny, V.; Ping, Y. How Spin Relaxes in Bulk Halide Perovskites. *Nat. Commun.* **2023**, in press.
(19) Xu, J.; Takenaka, H.; Habib, A.; Sundararaman, R.; Ping, Y. Giant Spin Lifetime Anisotropy and Spin-Valley Locking in Silicene and Germanene from First-Principles Density-Matrix Dynamics. *Nano Lett.* **2021**, *21*, 9594−9600.
(20) Habib, A.; Xu, J.; Ping, Y.; Sundararaman, R. Electric fields and substrates dramatically accelerate spin relaxation in graphene. *Phys. Rev. B* **2022**, *105*, No. 115122.
(21) Xu, J.; Ping, Y. Substrate effects on spin relaxation in two-dimensional Dirac materials with strong spin-orbit coupling. *npj Comput. Mater.* **2023**, *9*, 47.
(22) Rossi, F.; Kuhn, T. Theory of Ultrafast Phenomena in Photoexcited Semiconductors. *Rev. Mod. Phys.* **2002**, *74*, 895−950.
(23) Bonitz, M. *Quantum Kinetic Theory*; Springer, Cham, 2016; Chapter 2. DOI: 10.1007/978-3-319-24121-0.
(24) Axt, V. M.; Stahl, A. A dynamics-controlled truncation scheme for the hierarchy of density matrices in semiconductor optics. *Z. Physik B - Condensed Matter* **1994**, *93*, 195−204.
(25) Kikkawa, J. M.; Awschalom, D. D. Resonant Spin Amplification in n-Type GaAs. *Phys. Rev. Lett.* **1998**, *80*, 4313−4316.
(26) Yang, L.; Sinitsyn, N. A.; Chen, W.; Yuan, J.; Zhang, J.; Lou, J.; Crooker, S. A. Long-Lived Nanosecond Spin Relaxation and Spin Coherence of Electrons in Monolayer MoS2 and WS2. *Nat. Phys.* **2015**, *11*, 830−834.
(27) Iotti, R. C.; Rossi, F. Phonon-induced dissipation and decoherence in solid-state quantum devices: Markovian versus non-Markovian treatments. *Eur. Phys. J. B* **2017**, *90*, 250.
(28) Marini, A. Competition between the electronic and phonon−mediated scattering channels in the out−of−equilibrium carrier dynamics of semiconductors: an ab-initio approach. *Journal of Physics: Conference Series* **2013**, *427*, No. 012003.
(29) Hannewald, K.; Glutsch, S.; Bechstedt, F. Quantum-kinetic study of femtosecond pump-and-probe spectra of bulk GaAs. *Phys. Rev. B* **2000**, *61*, 10792−10802.
(30) Poncé, S.; Margine, E. R.; Giustino, F. Towards predictive many-body calculations of phonon-limited carrier mobilities in semiconductors. *Phys. Rev. B* **2018**, *97*, No. 121201.
(31) Kandolf, N.; Verdi, C.; Giustino, F. Many-body Green's function approaches to the doped Fröhlich solid: Exact solutions and anomalous mass enhancement. *Phys. Rev. B* **2022**, *105*, No. 085148.
(32) Kohn, W.; Luttinger, J. Quantum theory of electrical transport phenomena. *Phys. Rev.* **1957**, *108*, 590−611.
(33) Krieger, J.; Iafrate, G. Quantum transport for bloch electrons in a spatially homogeneous electric field. *Phys. Rev. B* **1987**, *35*, 9644−9658.
(34) Ciancio, E.; Iotti, R. C.; Rossi, F. Gauge-invariant formulation of high-field transport in semiconductors. *Phys. Rev. B* **2004**, *69*, No. 165319.
(35) Kané, G.; Lazzeri, M.; Mauri, F. Zener tunneling in the electrical transport of quasimetallic carbon nanotubes. *Phys. Rev. B* **2012**, *86*, No. 155433.
(36) Sekine, A.; Culcer, D.; MacDonald, A. H. Quantum kinetic theory of the chiral anomaly. *Phys. Rev. B* **2017**, *96*, No. 235134.
(37) Ventura, G. B.; Passos, D. J.; Lopes dos Santos, J. M. B.; Viana Parente Lopes, J. M.; Peres, N. M. R. Gauge covariances and nonlinear optical responses. *Phys. Rev. B* **2017**, *96*, No. 035431.
(38) Iafrate, G.; Sokolov, V.; Krieger, J. Quantum transport and the Wigner distribution function for Bloch electrons in spatially homogeneous electric and magnetic fields. *Phys. Rev. B* **2017**, *96*, No. 144303.
(39) King-Smith, R. D.; Vanderbilt, D. Theory of polarization of crystalline solids. *Phys. Rev. B* **1993**, *47*, 1651−1654.
(40) Resta, R. Macroscopic polarization in crystalline dielectrics: the geometric phase approach. *Rev. Mod. Phys.* **1994**, *66*, 899−915.
(41) Multunas, C.; Grieder, A.; Xu, J.; Ping, Y.; Sundararaman, R. Circular dichroism in crystals from first principles. *Phys. Rev. Mater.* **2023**, *7*, 123801.
(42) Rosati, R.; Iotti, R. C.; Dolcini, F.; Rossi, F. Derivation of Nonlinear Single-Particle Equations via Many-Body Lindblad Superoperators: A Density-Matrix Approach. *Phys, Rev. B* **2014**, *90*, No. 125140.
(43) Giustino, F. Electron-Phonon Interactions from First Principles. *Rev. Mod. Phys.* **2017**, *89*, No. 015003.
(44) Sundararaman, R.; Ping, Y. First-principles electrostatic potentials for reliable alignment at interfaces and defects. *J. Chem. Phys.* **2017**, *146*, No. 104109.
(45) Jacoboni, C. *Theory of Electron Transport in Semiconductors: A Pathway from Elementary Physics to Nonequilibrium Green Functions*; Springer Series in Solid-State Sciences, Vol. *165*; Springer Science & Business Media, 2010. DOI: 10.1007/978-3-642-10586-9.
(46) Xiao, C.; Du, Z.; Niu, Q. Theory of nonlinear Hall effects: Modified semiclassics from quantum kinetics. *Phys. Rev. B* **2019**, *100*, No. 165422.
(47) Kochan, D.; Gmitra, M.; Fabian, J. Spin relaxation mechanism in graphene: resonant scattering by magnetic impurities. *Phys. Rev. Lett.* **2014**, *112*, No. 116602.
(48) Lü, C.; Cheng, J.; Wu, M.; da Cunha Lima, I. Spin relaxation time, spin dephasing time and ensemble spin dephasing time in n-type GaAs quantum wells. *Phys. Lett. A* **2007**, *365*, 501−504.
(49) Meier, F.; Zakharchenya, B. P. *Optical Orientation*; Elsevier, 2012.
(50) Dean, M. P. M.; Cao, Y.; Liu, X.; Wall, S.; Zhu, D.; Mankowsky, R.; Thampy, V.; Chen, X. M.; Vale, J. G.; Casa, D.; et al. Ultrafast Energy-and Momentum-Resolved Dynamics of Magnetic Correlations in the Photo-Doped Mott Insulator Sr2IrO4. *Nat. Mater.* **2016**, *15*, 601−605.
(51) Kimel, A. V.; Bentivegna, F.; Gridnev, V. N.; Pavlov, V. V.; Pisarev, R. V.; Rasing, T. h. Room-Temperature Ultrafast Carrier and Spin Dynamics in GaAs Probed by the Photoinduced Magneto-Optical Kerr Effect. *Phys, Rev. B* **2001**, *63*, No. 235201.
(52) Molina-Sánchez, A.; Sangalli, D.; Wirtz, L.; Marini, A. Ab Initio Calculations of Ultrashort Carrier Dynamics in Two-Dimensional

Materials: Valley Depolarization in Single-Layer WSe2. *Nano Lett.* **2017**, *17*, 4549−4555.
(53) Mainkar, N.; Browne, D. A.; Callaway, J. First-Principles LCGO Calculation of the Magneto-Optical Properties of Nickel and Iron. *Phys, Rev. B* **1996**, *53*, 3692−3701.
(54) Sundararaman, R.; Letchworth-Weaver, K.; Schwarz, K. A.; Gunceler, D.; Ozhabes, Y.; Arias, T. A. JDFTx: Software for Joint Density-Functional Theory. *SoftwareX* **2017**, *6*, 278−284.
(55) Marzari, N.; Vanderbilt, D. Maximally Localized Generalized Wannier Functions for Composite Energy Bands. *Phys. Rev. B* **1997**, *56*, 12847−12865.
(56) Brown, A. M.; Sundararaman, R.; Narang, P.; Goddard, W. A.; Atwater, H. A. Nonradiative Plasmon Decay and Hot Carrier Dynamics: Effects of Phonons, Surfaces, and Geometry. *ACS Nano* **2016**, *10*, 957−966.
(57) Narang, P.; Zhao, L.; Claybrook, S.; Sundararaman, R. Effects of Interlayer Coupling on Hot Carrier Dynamics in Graphene-Derived van der Waals Heterostructures. *Adv. Opt. Mater.* **2017**, *5*, No. 1600914.
(58) Brown, A. M.; Sundararaman, R.; Narang, P.; Schwartzberg, A. M.; Goddard, W. A., III; Atwater, H. A. Experimental and Ab Initio Ultrafast Carrier Dynamics in Plasmonic Nanoparticles. *Phys. Rev. Lett.* **2017**, *118*, No. 087401.
(59) Habib, A.; Florio, R.; Sundararaman, R. Hot Carrier Dynamics in Plasmonic Transition Metal Nitrides. *J. Opt.* **2018**, *20*, No. 064001.
(60) Brown, A. M.; Sundararaman, R.; Narang, P.; Goddard, W. A., III; Atwater, H. A. Ab Initio Phonon Coupling and Optical Response of Hot Electrons in Plasmonic Metals. *Phys. Rev. B* **2016**, *94*, No. 075120.
(61) Verdi, C.; Giustino, F. Fröhlich Electron-Phonon Vertex from First Principles. *Phys. Rev. Lett.* **2015**, *115*, No. 176401.
(62) Sohier, T.; Gibertini, M.; Calandra, M.; Mauri, F.; Marzari, N. Breakdown of optical phonons' splitting in two-dimensional materials. *Nano Lett.* **2017**, *17*, 3758−3763.
(63) Iotti, R. C.; Rossi, F. Nature of charge transport in quantum-cascade lasers. *Phys. Rev. Lett.* **2001**, *87*, No. 146603.
(64) Watanabe, H.; Yanase, Y. Chiral photocurrent in parity-violating magnet and enhanced response in topological antiferromagnet. *Phys. Rev. X* **2021**, *11*, No. 011001.
(65) Rosati, R.; Rossi, F. Quantum diffusion due to scattering non-locality in nanoscale semiconductors. *Europhys. Lett.* **2014**, *105*, No. 17010.
(66) Simoncelli, M.; Marzari, N.; Mauri, F. Wigner formulation of thermal transport in solids. *Phys. Rev. X* **2022**, *12*, No. 041011.
(67) Kubo, R. The fluctuation-dissipation theorem. *Rep. Prog. Phys.* **1966**, *29*, 255.
(68) Maassen, T.; Dejene, F.; Guimarães, M.; Józsa, C.; Van Wees, B. Comparison between charge and spin transport in few-layer graphene. *Phys. Rev. B* **2011**, *83*, No. 115410.
(69) Ciccarino, C. J.; Christensen, T.; Sundararaman, R.; Narang, P. Dynamics and spin-valley locking effects in monolayer transition metal dichalcogenides. *Nano Lett.* **2018**, *18*, 5709−5715.
(70) Gunst, T.; Markussen, T.; Stokbro, K.; Brandbyge, M. First-principles method for electron-phonon coupling and electron mobility: Applications to two-dimensional materials. *Phys. Rev. B* **2016**, *93*, No. 035414.
(71) Mahan, G. D. *Many-Particle Physics*; Springer US, 2000.
(72) Balzer, K.; Bonitz, M. *Nonequilibrium Green's Functions Approach to Inhomogeneous Systems*; Springer, 2012. DOI: 10.1007/978-1-4757-5714-9.
(73) Attaccalite, C.; Grüning, M.; Marini, A. Real-time approach to the optical properties of solids and nanostructures: Time-dependent Bethe-Salpeter equation. *Phys. Rev. B* **2011**, *84*, No. 245110.
(74) Chan, Y.-H.; Qiu, D. Y.; da Jornada, F. H.; Louie, S. G. Giant exciton-enhanced shift currents and direct current conduction with subbandgap photo excitations produced by many-electron interactions. *Proc. Natl. Acad. Sci. U .S. A.* **2021**, *118*, No. e1906938118.
(75) Elliott, P.; Stamenova, M.; Simoni, J.; Sharma, S.; Sanvito, S.; Gross, E. K. U. In *Handbook of Materials Modeling: Methods: Theory and Modeling*; Andreoni, W., Yip, S., Eds.; Springer International: Cham, Switzerland, 2020; pp 841−866. DOI: 10.1007/978-3-319-42913-7_70-1.
(76) Xiao, D.; Chang, M.-C.; Niu, Q. Berry phase effects on electronic properties. *Rev. Mod. Phys.* **2010**, *82*, 1959−2007.
(77) Groth, C. W.; Wimmer, M.; Akhmerov, A. R.; Waintal, X. Kwant: a software package for quantum transport. *New J. Phys.* **2014**, *16*, No. 063065.
(78) Vila, M.; Hsu, C.-H.; Garcia, J. H.; Benítez, L. A.; Waintal, X.; Valenzuela, S. O.; Pereira, V. M.; Roche, S. Low-symmetry topological materials for large charge-to-spin interconversion: The case of transition metal dichalcogenide monolayers. *Phys. Rev. Res.* **2021**, *3*, No. 043230.
(79) Wesselink, R. J.; Gupta, K.; Yuan, Z.; Kelly, P. J. Calculating spin transport properties from first principles: Spin currents. *Phys. Rev. B* **2019**, *99*, No. 144409.
(80) Belashchenko, K. D.; Kovalev, A. A.; van Schilfgaarde, M. Theory of spin loss at metallic interfaces. *Phys. Rev. Lett.* **2016**, *117*, No. 207204.
(81) Rojas, W. Y.; Villegas, C. E.; Rocha, A. R. Ab initio modelling of spin relaxation lengths in disordered graphene nanoribbons. *Phys. Chem. Chem. Phys.* **2019**, *21*, 26027−26032.
(82) Egami, Y.; Tsukamoto, S.; Ono, T. Calculation of the Green's function in the scattering region for first-principles electron-transport simulations. *Phys. Rev. Res.* **2021**, *3*, No. 013038.
(83) Fabian, J.; Das Sarma, S. Spin relaxation of conduction electrons in polyvalent metals: Theory and a realistic calculation. *Phys. Rev. Lett.* **1998**, *81*, 5624.
(84) Leyland, W.; Harley, R.; Henini, M.; Shields, A.; Farrer, I.; Ritchie, D. Oscillatory Dyakonov-Perel spin dynamics in two-dimensional electron gases. *Phys. Rev. B* **2007**, *76*, No. 195305.
(85) Yafet, Y. *Solid state physics*; Elsevier, 1963; Vol. *14*; pp 1−98. DOI: 10.1016/S0081-1947(08)60259-3.
(86) Yu, Z. Effective-mass model and magneto-optical properties in hybrid perovskites. *Sci. Rep.* **2016**, *6*, No. 28576.
(87) Kirstein, E.; et al. The Landé factors of electrons and holes in lead halide perovskites: universal dependence on the band gap. *Nat. Commun.* **2022**, *13*, 3062.
(88) Lepine, D. J. Spin-dependent recombination on silicon surface. *Phys. Rev. B* **1972**, *6*, 436−441.
(89) Huang, B.; Monsma, D. J.; Appelbaum, I. Coherent spin transport through a 350 micron thick silicon wafer. *Phys. Rev. Lett.* **2007**, *99*, No. 177209.
(90) Haag, M.; Illg, C.; Fähnle, M. Role of electron-magnon scatterings in ultrafast demagnetization. *Phys. Rev. B* **2014**, *90*, No. 014417.
(91) Müller, M. C.; Blügel, S.; Friedrich, C. Electron-magnon scattering in elementary ferromagnets from first principles: Lifetime broadening and band anomalies. *Phys. Rev. B* **2019**, *100*, No. 045130.
(92) Lischner, J.; Bazhirov, T.; MacDonald, A. H.; Cohen, M. L.; Louie, S. G. Effect of spin fluctuations on quasiparticle excitations: First-principles theory and application to sodium and lithium. *Phys. Rev. B* **2014**, *89*, No. 081108.
(93) Dey, P.; Yang, L.; Robert, C.; Wang, G.; Urbaszek, B.; Marie, X.; Crooker, S. A. Gate-Controlled Spin-Valley Locking of Resident Carriers in WSe2Monolayers. *Phys. Rev. Lett.* **2017**, *119*, No. 137401.
(94) Li, J.; Goryca, M.; Yumigeta, K.; Li, H.; Tongay, S.; Crooker, S. A. Valley relaxation of resident electrons and holes in a monolayer semiconductor: Dependence on carrier density and the role of substrate-induced disorder. *Phys. Rev. Mater.* **2021**, *5*, No. 044001.
(95) Goryca, M.; Wilson, N. P.; Dey, P.; Xu, X.; Crooker, S. A. Detection of thermodynamic "valley noise" in monolayer semiconductors: Access to intrinsic valley relaxation time scales. *Sci. Adv.* **2019**, *5*, No. eaau4899.
(96) Song, X.; Xie, S.; Kang, K.; Park, J.; Sih, V. Long-lived hole spin/valley polarization probed by Kerr rotation in monolayer WSe2. *Nano Lett.* **2016**, *16*, 5010−5014.
(97) Yan, T.; Yang, S.; Li, D.; Cui, X. Long valley relaxation time of free carriers in monolayer WSe 2. *Phys. Rev. B* **2017**, *95*, No. 241406.

(98) Edelberg, D.; Rhodes, D.; Kerelsky, A.; Kim, B.; Wang, J.; Zangiabadi, A.; Kim, C.; Abhinandan, A.; Ardelean, J.; Scully, M.; et al. Approaching the intrinsic limit in transition metal diselenides via point defect control. *Nano Lett.* **2019**, *19*, 4371−4379.
(99) Rhodes, D.; Chae, S. H.; Ribeiro-Palau, R.; Hone, J. Disorder in van der Waals heterostructures of 2D materials. *Nat. Mater.* **2019**, *18*, 541−549.
(100) Yankowitz, M.; McKenzie, D.; LeRoy, B. J. Local spectroscopic characterization of spin and layer polarization in WSe 2. *Phys. Rev. Lett.* **2015**, *115*, No. 136803.
(101) Tao, L.; Tsymbal, E. Y. Two-dimensional spin-valley locking spin valve. *Phys. Rev. B* **2019**, *100*, No. 161110.
(102) Hilton, D. J.; Tang, C. L. Optical Orientation and Femtosecond Relaxation of Spin-Polarized Holes in GaAs. *Phys. Rev. Lett.* **2002**, *89*, No. 146601.
(103) Jiang, J. H.; Wu, M. W. Electron-Spin Relaxation in Bulk III-V Semiconductors from a Fully Microscopic Kinetic Spin Bloch Equation Approach. *Phys, Rev. B* **2009**, *79*, No. 125206.
(104) Kamra, A.; Ghosh, B. The Role of Electron-Electron Scattering in Spin Transport. *J. Appl. Phys.* **2011**, *109*, No. 024501.
(105) Dettwiler, F.; Fu, J.; Mack, S.; Weigele, P. J.; Egues, J. C.; Awschalom, D. D.; Zumbühl, D. M. Stretchable Persistent Spin Helices in GaAs Quantum Wells. *Phys. Rev. X* **2017**, *7*, No. 031010.
(106) Huber, D.; Reindl, M.; Covre da Silva, S. F.; Schimpf, C.; Martin-Sanchez, J.; Huang, H.; Piredda, G.; Edlinger, J.; Rastelli, A.; Trotta, R. Strain-Tunable GaAs Quantum Dot: A Nearly Dephasing-Free Source of Entangled Photon Pairs on Demand. *Phys. Rev. Lett.* **2018**, *121*, No. 033902.
(107) Belykh, V. V.; Kuntsevich, A. Y.; Glazov, M. M.; Kavokin, K. V.; Yakovlev, D. R.; Bayer, M. Quantum Interference Controls the Electron Spin Dynamics in n-GaAs. *Phys. Rev. X* **2018**, *8*, No. 031021.
(108) Ohno, Y.; Terauchi, R.; Adachi, T.; Matsukura, F.; Ohno, H. Spin Relaxation in GaAs (110) Quantum wells. *Phys. Rev. Lett.* **1999**, *83*, 4196−4199.
(109) Hohage, P. E.; Bacher, G.; Reuter, D.; Wieck, A. D. Coherent Spin Oscillations in Bulk GaAs at Room Temperature. *Appl. Phys. Lett.* **2006**, *89*, No. 231101.
(110) Yu, Z. G.; Krishnamurthy, S.; Van Schilfgaarde, M.; Newman, N. Spin Relaxation of Electrons and Holes in Zinc-Blende Semiconductors. *Phys, Rev. B* **2005**, *71*, No. 245312.
(111) Mower, M. D.; Vignale, G.; Tokatly, I. V. Dyakonov-Perel Spin Relaxation for Degenerate Electrons in the Electron-Hole Liquid. *Phys, Rev. B* **2011**, *83*, No. 155205.
(112) Marchetti, G.; Hodgson, M.; McHugh, J.; Chantrell, R.; D'Amico, I. Spin Relaxation in GaAs: Importance of Electron-Electron Interactions. *Materials* **2014**, *7*, 2795−2814.
(113) Drogeler, M.; Franzen, C.; Volmer, F.; Pohlmann, T.; Banszerus, L.; Wolter, M.; Watanabe, K.; Taniguchi, T.; Stampfer, C.; Beschoten, B. Spin lifetimes exceeding 12 ns in graphene nonlocal spin valve devices. *Nano Lett.* **2016**, *16*, 3533−3539.
(114) Dean, C. R.; Young, A. F.; Meric, I.; Lee, C.; Wang, L.; Sorgenfrei, S.; Watanabe, K.; Taniguchi, T.; Kim, P.; Shepard, K. L.; Hone, J. Boron Nitride Substrates for High-quality Graphene Electronics. *Nat. Nanotechnol.* **2010**, *5*, 722−726.
(115) Han, W.; Kawakami, R. K. Spin relaxation in single-layer and bilayer graphene. *Phys. Rev. Lett.* **2011**, *107*, No. 047207.
(116) Guimarães, M. H.; Zomer, P. J.; Ingla-Aynés, J.; Brant, J. C.; Tombros, N.; van Wees, B. J. Controlling spin relaxation in hexagonal BN-encapsulated graphene with a transverse electric field. *Phys. Rev. Lett.* **2014**, *113*, No. 086602.
(117) Raes, B.; Scheerder, J. E.; Costache, M. V.; Bonell, F.; Sierra, J. F.; Cuppens, J.; Van de Vondel, J.; Valenzuela, S. O. Determination of the Spin-Lifetime Anisotropy in Graphene Using Oblique Spin Precession. *Nat. Commun.* **2016**, *7*, No. 11444.
(118) Guimarães, M. H.; Veligura, A.; Zomer, P.; Maassen, T.; Vera-Marun, I.; Tombros, N.; Van Wees, B. Spin transport in high-quality suspended graphene devices. *Nano Lett.* **2012**, *12*, 3512−3517.
(119) Cummings, A. W.; Garcia, J. H.; Fabian, J.; Roche, S. Giant Spin Lifetime Anisotropy in Graphene Induced by Proximity Effects. *Phys. Rev. Lett.* **2017**, *119*, No. 206601.
(120) Zomer, P. J.; Guimarães, M. H. D.; Tombros, N.; van Wees, B. J. Long-Distance Spin Transport in High-Mobility Graphene on Hexagonal Boron Nitride. *Phys. Rev. B* **2012**, *86*, No. 161416.
(121) Kamalakar, M. V.; Groenveld, C.; Dankert, A.; Dash, S. P. Long distance spin communication in chemical vapour deposited graphene. *Nat. Commun.* **2015**, *6*, 6766.
(122) Zollner, K.; Gmitra, M.; Fabian, J. Heterostructures of Graphene and HBN: Electronic, Spin-Orbit, and Spin Relaxation Properties from First Principles. *Phys. Rev. B* **2019**, *99*, No. 125151.
(123) Van Tuan, D.; Ortmann, F.; Cummings, A. W.; Soriano, D.; Roche, S. Spin dynamics and relaxation in graphene dictated by electron-hole puddles. *Sci. Rep.* **2016**, *6*, No. 21046.
(124) Paleari, F.; Marini, A. Exciton-phonon interaction calls for a revision of the "exciton" concept. *Phys. Rev. B* **2022**, *106*, No. 125403.
(125) Guo, C.; Xu, J.; Ping, Y. Substrate effect on excitonic shift and radiative lifetime of two-dimensional materials. *J. Condens. Matter Phys.* **2021**, *33*, No. 234001.
(126) Wu, F.; Rocca, D.; Ping, Y. Dimensionality and anisotropicity dependence of radiative recombination in nanostructured phosphorene. *J. Mater. Chem. C* **2019**, *7*, 12891−12897.
(127) Smart, T. J.; Li, K.; Xu, J.; Ping, Y. Intersystem crossing and exciton−defect coupling of spin defects in hexagonal boron nitride. *npj Comput. Mater.* **2021**, *7*, 59.
(128) Antonius, G.; Louie, S. G. Theory of exciton-phonon coupling. *Phys. Rev. B* **2022**, *105*, No. 085111.
(129) Chen, H.-Y.; Sangalli, D.; Bernardi, M. Exciton-phonon interaction and relaxation times from first principles. *Phys. Rev. Lett.* **2020**, *125*, No. 107401.
(130) Watanabe, H.; Yanase, Y. Chiral Photocurrent in Parity-Violating Magnet and Enhanced Response in Topological Antiferromagnet. *Phys. Rev. X* **2021**, *11*, No. 011001.
(131) De Juan, F.; Grushin, A. G.; Morimoto, T.; Moore, J. E. Quantized circular photogalvanic effect in Weyl semimetals. *Nat. Commun.* **2017**, *8*, No. 15995.
(132) Hellman, O.; Steneteg, P.; Abrikosov, I. A.; Simak, S. I. Temperature dependent effective potential method for accurate free energy calculations of solids. *Phys. Rev. B* **2013**, *87*, No. 104111.
(133) Macheda, F.; Barone, P.; Mauri, F. Electron-phonon interaction and longitudinal-transverse phonon splitting in doped semiconductors. *Phys. Rev. Lett.* **2022**, *129*, No. 185902.
(134) Han, W.; Kawakami, R. K.; Gmitra, M.; Fabian, J. Graphene spintronics. *Nat. Nanotechnol.* **2014**, *9*, 794−807.
(135) Li, Y.; Chen, P.; Zhou, G.; Li, J.; Wu, J.; Gu, B.-L.; Zhang, S.; Duan, W. Dirac fermions in strongly bound graphene systems. *Phys. Rev. Lett.* **2012**, *109*, No. 206802.
(136) Bao, C.; Zhang, H.; Zhang, T.; Wu, X.; Luo, L.; Zhou, S.; Li, Q.; Hou, Y.; Yao, W.; Liu, L.; et al. Experimental evidence of chiral symmetry breaking in Kekulé-ordered graphene. *Phys. Rev. Lett.* **2021**, *126*, No. 206804.
(137) Xuan, F.; Quek, S. Y. Valley Zeeman effect and Landau levels in two-dimensional transition metal dichalcogenides. *Phys. Rev. Res.* **2020**, *2*, No. 033256.
(138) Tao, L.; Tsymbal, E. Y. Persistent spin texture enforced by symmetry. *Nat. Commun.* **2018**, *9*, 2763.
(139) Ai, H.; Ma, X.; Shao, X.; Li, W.; Zhao, M. Reversible out-of-plane spin texture in a two-dimensional ferroelectric material for persistent spin helix. *Phys. Rev. Mater.* **2019**, *3*, No. 054407.
(140) Towns, J.; Cockerill, T.; Dahan, M.; Foster, I.; Gaither, K.; Grimshaw, A.; Hazlewood, V.; Lathrop, S.; Lifka, D.; Peterson, G. D.; Roskies, R.; Scott, J. R.; Wilkins-Diehr, N. XSEDE: Accelerating Scientific Discovery. *Comput. Sci. Eng.* **2014**, *16*, 62−74.

https://doi.org/10.1021/acs.jctc.3c00598
J. Chem. Theory Comput. 2024, 20, 492−512